THE β^- DECAY OF ^{44}Cl

By

Hatim Hanafi Yousif

A Thesis
Submitted to the Faculty of
Mississippi State University
in Partial Fulfillment of the Requirements
for the Degree of Master of Science
in Physics
in the Department of Physics and Astronomy

Mississippi State, Mississippi

December 2003

UMI Number: 1416727

INFORMATION TO USERS

The quality of this reproduction is dependent upon the quality of the copy submitted. Broken or indistinct print, colored or poor quality illustrations and photographs, print bleed-through, substandard margins, and improper alignment can adversely affect reproduction.

In the unlikely event that the author did not send a complete manuscript and there are missing pages, these will be noted. Also, if unauthorized copyright material had to be removed, a note will indicate the deletion.

UMI®

UMI Microform 1416727

Copyright 2004 by ProQuest Information and Learning Company.

All rights reserved. This microform edition is protected against unauthorized copying under Title 17, United States Code.

ProQuest Information and Learning Company
300 North Zeeb Road
P.O. Box 1346
Ann Arbor, MI 48106-1346

THE β^- DECAY OF ^{44}Cl

By

Hatim Hanafi Yousif

Approved:

Jeffry A. Winger
Professor of Physics
(Director of Thesis)

Wenchao Ma

Wenchao Ma
Professor of Physics
(Committee Member)

Jim A. Dunne
Associate Professor of Physics
(Committee Member)

David L. Monts.

David L. Monts
Professor of Physics
Graduate Coordinator of the Department of Physics and Astronomy

Phil Oldham
Dean of the College of Arts and Science

Name: Hatim Hanafi Yousif

Date of Degree: December 13, 2003

Institution: Mississippi State University

Major Field: Physics

Major Professor: Dr. Jeff Winger

Title of Study: THE β^- DECAY OF ^{44}Cl

Pages in Study: 85

Candidate for Degree of Master of Science

Several experiments were conducted at the National Superconducting Cyclotron Laboratory (NSCL) at Michigan State University, to study exotic nuclei far from stability. Information about the structure of these nuclei has been limited until recently due to the difficulty in producing these nuclei. However, with the recent use of the projectile fragmentation facilities, these nuclei can be produced, separated, and studied in detail using several different techniques.

This study "THE β^- DECAY OF ^{44}Cl" was based on an experiment conducted at the NSCL. In this study, the β decay of ^{44}Cl into excited states ^{44}Ar has been studied for the first time. Many gamma rays were observed and a level scheme for ^{44}Ar up to 5351 keV has been established.

DEDICATION

I would like to dedicate this thesis to my family: my father Hanafi Y. Ali, my mother Safieah M. Ali, my brothers and sisters for their love, inspiration, and prayers.

ACKNOWLEDGEMENTS

I would like to express my sincerest appreciation to my major advisor, Dr. Jeffry A. Winger. His transcendental help, understanding, patience, and guidance made this work possible.

My gratitude is owed to the members of my thesis committee: Dr. Wenchao Ma, and Dr. Jim Dunne for their cooperation and advice.

A great deal of debt is owed to Dr. L. C. Croft for his encouragement and his invaluable remarks during the correction phase of this thesis.

I would like to thank all my teachers and professors throughout the various levels of my education. Their contribution in making the learning process a worthwhile and an enjoyable experience will never be forgotten. A note of thanks is extended to Connie and Amy at the Department of Physics for their help and support.

I would like to lovingly thank my family and my friends for their encouragement and support. Their incessant back-up made me make it to the finish line.

All thanks and praises, indeed, are due to Allah, for among His countless blessings and bounties that He bestowed upon me is the completion of this thesis.

TABLE OF CONTENTS

Page

DEDICATION ii

ACKNOWLEDGEMENTS iii

LIST OF TABLES iv

CHAPTER

I. INTRODUCTION 2
    Previous Work 2

II. THEORETICAL BACKGROUND 6
    2.1 The Shell Model 6
        2.1.1 Shell Model Potential 6
        2.1.2 Spin-Orbit Coupling 7
        2.1.3 Excited States 9
    2.2 The Nilsson Model 11
    2.3 The Collective Model 16
        2.3.1 The Vibrational Motion 16
        2.3.2 Deformed Nuclei 20
        2.3.3 The Rotational Motion 22
    2.4 Understanding ^{44}Ar 23

III. EXPERIMENTAL DETAILS 25
    3.1 Introduction 25
    3.2 Experimental Equipment 25
        3.2.1 The K1200 Cyclotron 25
        3.2.2 Design and Characteristics of A1200 Fragment Separator 26
        3.2.3 The Reaction Product Mass Separator (RPMS) 27

CHAPTER Page

3.3 Reaction and Detector Set up 27
3.4 Energy and Efficiency Calibration 33
3.5 Experimental Results 41

IV. DATA ANALYSIS 42

4.1 Branching Ratio 42
4.2 γ Ray Spectra and Coincidence Relationships 47
4.3 Half-life of ^{44}Cl 52

V. LEVEL SCHEME DEVELOPMENT 53

5.1 Introduction 53
5.2 Ground State of ^{44}Cl 56
5.3 Level Structure of ^{44}Ar 57
    I) Level at 1157 57
    II) Level at 2010 57
    III) Level at 2745 58
    IV) level at 2975 59
    V) Level at 4807 59
    VI) Level at 5351 60

VI. DISCUSSION AND CONCLUSION 61

6.1 Comparisons with Shell Model Studies of ^{44}Ar 61
6.2 Comparison between ^{42}Ar and ^{44}Ar 63
6.3 Summary and Conclusion 65

REFERENCES 67

APPENDIX

A. Electronics and logic circuitry 70

B. Programming Code for the Wheel Motor Control 76

LIST OF TABLES

TABLE Page

4.1 The “f” values calculated from γ rays from ^{44}Ar and ^{44}K decay relative to the intensity of 1157 keV from ^{44}Cl decay. The energy 1157 keV is the reference γ ray from ^{44}Cl. The terms in the caption are defined in the text 46

5.1 Energies of the γ rays placed in the ^{44}Ar level scheme, their relative intensities, their placements, and their coincidence relationships 54

5.2 Energy levels and corresponding spin/parity, feeding, and log(ft) values 56

LIST OF FIGURES

FIGURE Page

1.1 Comparison of the excited states in ^{44}Ar from the theoretical calculations of Retamosa *et al* [14] and the experimentally observed levels of S. Wan *et al* [15] 4

2.1 Single Particle energy levels showing the splitting due to the spin-orbit effect [19] 9

2.2 Diagram showing the motion of a particle around a prolate deformed nucleus. Quantities j, K, and θ are discussed in the text [Casten, Ref. 20, page 333] 12

2.3 Nilsson diagram for Z, N $\leq$ 50 region. The deformation parameter $\varepsilon(\approx 0.95\beta)$ is the abscissa. The ordinate units, $\hbar\omega_0$, are given approximately by $41 A^{1/3}$ MeV. [21] 15

2.4 The first three vibrational modes of a nucleus. Solid lines show the view of the vibrating surface, where as the dashed lines the spherical equilibrium of the nucleus. Figure taken from Krane [Ref. 18, page 140] 17

2.5 Schematic diagram showing how nuclear deformations depend on the value of β . Arrows indicate the symmetry axis [Casten [20] page 198] 21

3.1 Schematic layout of the A1200 28

3.2 Schematic layout of the detector endstation including particle tracking and identification detectors, rotating wheel into which the radioactive beam was implanted, two β detectors and two Ge detectors 29

FIGURE Page

3.3 Particle identification plots (ΔE versus TOF). The purity of the beam is controlled by the A1200 setting. Top is the setting for ^{41}P, bottom is that for ^{44}Cl. Small changes in the A1200 setting can result in very pure beams 31

3.4 The low energy calibration for the Ge-1 detector (gain $\approx$ 0.5 keV/channel). The upper section shows the energy difference between the known energies and a linear fit to the data. The lower section shows the difference between the known energies and the final fit. The dashed lines indicate the limits (1σ) of the intrinsic uncertainty in the fit................ 34

3.5 The high energy calibration for the Ge-1 detector (gain $\approx$ 1.0 keV/channel). The upper section shows the energy difference between the known energies and a linear fit to the data. The lower section shows the difference between the known energies and the final fit. The dashed lines indicate the limits (1σ) of the intrinsic uncertainty in the fit................. 35

3.6 The low energy calibration for the Ge-2 detector (gain $\approx$ 0.5 keV/channel). The upper section shows the energy difference between the known energies and a linear fit to the data. The lower section shows the difference between the known energies and the final fit. The dashed lines indicate the limits (1σ) of the intrinsic uncertainty in the fit................ 36

3.7 The high energy calibration for the Ge-2 detector (gain $\approx$ 1.0 keV/channel). The upper section shows the energy difference between the known energies and a linear fit to the data. The lower section shows the difference between the known energies and the final fit. The dashed lines indicate the limits (1σ) of the intrinsic uncertainty in the fit................. 37

3.8 Efficiency calibration spectra for the Ge-1 detector. The upper section shows the log-log plot of efficiency versus energy. The solid line shows the fit photopeak efficiency curve, and the dashed line shows the total efficiency curve. The lower section shows the uncertainty in the calibration as a function of energy in log- log scale 39

FIGURE Page

3.9 Efficiency calibration spectra for the Ge-2 detector. The upper section shows the log-log plot of efficiency versus energy. The solid line shows the fit photopeak efficiency curve, and the dashed line shows the total efficiency curve. The lower section shows the uncertainty in the calibration as a function of energy in log- log scale 40

4.1 Partial level scheme of ^{44}Ar decay into ^{44}K showing the 1703- and 1886-keV γ rays used in determining the "f" value for the ^{44}Cl 43

4.2 Partial level scheme of ^{44}K decay into ^{44}Ca showing the 1157-, 1126-, 1499-, 1024-, and 2518-keV γ rays used in determining the "f" value for the ^{44}Cl decay 44

4.3 β-gated γ-ray singles spectrum for the Ge-1 detector. Lines assigned to the decay of ^{44}Cl decay are labeled with their energy in keV. Single Escape Peaks (SEP) are labeled with the energy of the original γ ray followed by SEP 49

4.4 Background–subtracted γ ray coincidence spectra gated on the 852, 1157, 2110 and 2796 keV 50

4.5 Background–subtracted γ ray coincidence spectra gated on the 965, 1587, 1817, 2376 and 3338 keV 51

4.6 Half-life curve for the decay of the 852 and 2010, and 2796 keV γ rays associated with ^{44}Cl β decay 52

5.1 Level scheme for ^{44}Ar as determined from ^{44}Cl β decay. The width of the transition is proportional to the relative intensity of the γ ray.. 55

6.1 Comparison of the level scheme of ^{44}Ar to the theoretical calculations [15,16]. Excitation energies are in keV 62

6.2 Comparison of the level scheme of ^{44}Ar to the level scheme of ^{42}Ar [7].. 64

FIGURE Page

A.1 Schematic diagram of the beam monitoring electronics and logic circuitry, and mastergate logic circuitry 72

A.2 Schematic diagram of β1 detector electronics and logic circuitry 73

A.3 Schematic diagram of β2 detector electronics and logic circuitry 74

A.3 Schematic diagram of the germanium detector electronics and logic circuitry 75

CHAPTER I

INTRODUCTION

The Pauli exclusion principle, which states that no two fermions can occupy the same quantum state, i.e. have identical sets of quantum numbers, requires that a finite number of such particles occupy a given energy level, which led to the concept of closed levels or shells. Numerous experiments support the concept that nuclei manifest periodic structure, indicating that closed shells occur at neutron or proton numbers of 8, 20, 28, 50, 82, and 126, the so called magic numbers [1]. The nuclei ${}^{48}_{20}Ca_{28}$, ${}^{40}_{20}Ca_{20}$, and ${}^{16}_{8}O_{8}$ are good examples of the exceptional stability of "doubly magic" nuclei since they have both a magic number of protons and a magic number of neutrons [2]. Away from stability, however, some magic numbers disappear and new magic numbers appear. Understanding this phenomenon requires additional study.

In the mid 1970's, X. Campi *et al* [3], upon studying the shape transition in the neutron rich sodium isotopes, proposed that the sodium isotopes in this mass region are strongly deformed due to the filling of negative parity orbits from the $\nu 1f_{7/2}$ shell. Another study by T. Motobayashi *et al.* suggested, now supported by theoretical calculations, the picture of large deformation and a vanishing N=20 shell gap in ^{32}Mg [4]. T. R. Werner *et al.* [5] in theoretical studies of the ground state properties of exotic Si, S, Ar, and Ca isotopes, particularly those with neutron number around the magic neutron number 28 ($^{40\text{-}44}$Si, $^{40\text{-}44}$S), and the heaviest isotopes close to the neutron drip line ($^{58\text{-}70}$Ca), have suggested strong deformation.

Experiments performed at the National Superconducting Laboratory (NSCL) at Michigan State University have confirmed that a region of deformation exists near the N=28 nucleus ^{44}S. The first evidence of this moderate deformation near N=28 was presented by H. Scheit *et al.* [6] in an experiment conducted at the NSCL in which measurements of the energy and reduced transition probability, B(E2; $0^+_{\text{g.s.}} \rightarrow 2^+$), of the lowest 2^+ state in the neutron- rich radioactive nuclei ^{38,40,42}S and ^{44,46}Ar were made using the technique of intermediate–energy Coulomb excitation. In a complimentary experiment, a measurement of the β-decay of ^{40}P to determine the half-life and the structure of the daughter nucleus ^{40}S was conducted at the NSCL by Winger *et al.* [7]. This experiment has shown the possibility of using the NSCL facilities for performing detailed decay scheme measurements.

Previous Work

Early experiments on the β-decay of exotic nuclei in the N=20 to 28 and Z=10 to 20 region performed at various labs concentrated on half-life measurements and β-delayed neutron probabilities. A study by R. E. Larson and C. M. Gordon in the late 1960's showed, for the first time, the production of ^{44}Ar with a half life of 14.0 ± 1.5 min by the ^{48}Ca(γ, α) ^{44}Ar reaction. The observed γ-ray associated with the decay of ^{44}Ar was measured to be 1886.5 ± 0.8 keV [8]. At the CERN 600 MeV synchro-cyclotron, using the reaction $^{nat}V(p, \text{spallation})\ ^{44}Ar$, a study by J. Hudis, E. Hagebø, and P. Patzelt measured the half life of ^{44}Ar as 11.87 ± 0.05 min, with only five γ-rays accompanying its decay, namely: 182.3 ± 0.1 keV, 406.3±0.5 keV, 427.6 ± 1.0 keV, 1704.7 ± 0.4 keV, and 1886.7 ± 0.5 keV [9]. In the mid 1970's, G. M Crawley *et al.* measured the mass excess and some energy levels of the nuclide ^{44}Ar using the reaction $^{48}Ca(^{3}He, ^{7}Be)\ ^{44}Ar$. The mass excess of ^{44}Ar was found to be –32.27 ± 0.02 MeV, and the energy levels observed were: 0.75 ± 0.03 MeV, 1.61 ± 0.03 MeV, 3.48 ± 0.03 MeV, 3.98 ± 0.05 MeV, and 4.43 ± 0.04 MeV [10]. Zhou *et al.*, in their direct mass measurements of the neutron-rich isotopes of chlorine through iron and then fluorine through chlorine, found the mass excess of ^{44}Cl to be –20.0 ± 0.5 and -19.98 ± 0.25 MeV, respectively [11,12]. Among the very few studies on ^{44}Cl was a measurement by Sorlin *et al.* of the β-decay of nuclei far from stability near N=28 in which the measurement of the half-life and β-delayed neutron emission of ^{44}Cl were found to be 434 ± 60 ms and <8%, respectively [13]. Retamosa *et al.* [14] in a shell model study of the neutron-rich nuclei around N=28 calculated an energy of 1182 keV for the 2_1^+ state of ^{44}Ar. S. Wan *et al.* [15] studied the nuclear structure of the neutron-rich nuclei below ^{48}Ca between the two magic numbers 20 and 28 using the experimental method of in-beam γ-spectroscopy with relativistic radioactive beams. A comparison of the proposed energy level schemes of ^{44}Ar between the experimentally observed and theoretical calculations extended by Retamosa *et al.* is shown in Fig.1.1.

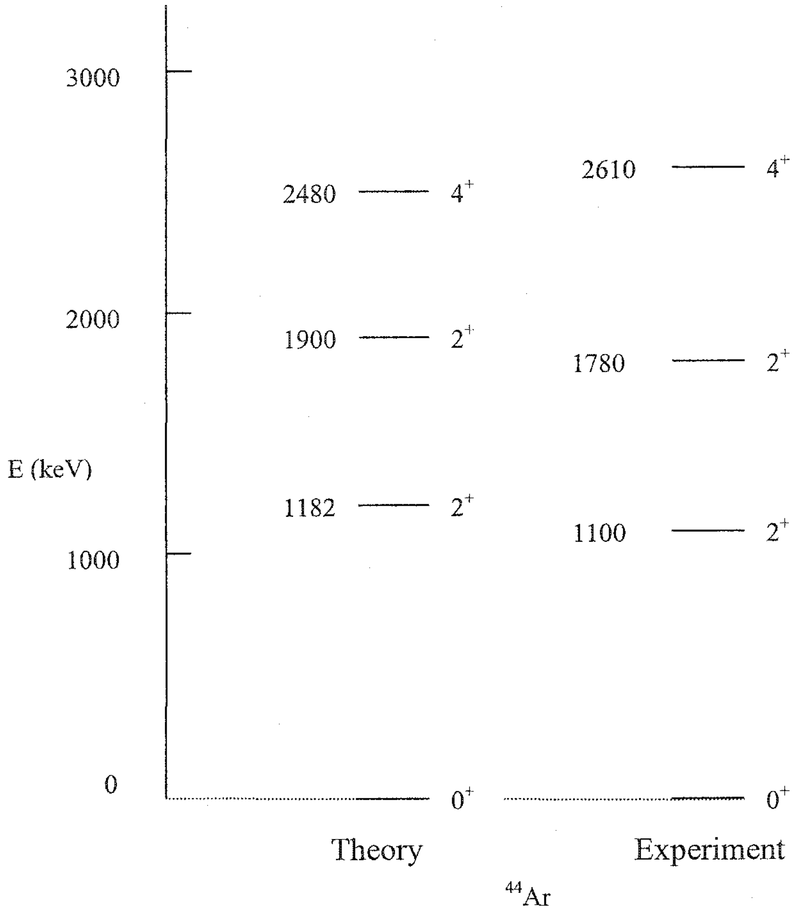
3000
2000
1000
0
E (keV)
2480 4+
1900 2+
1182 2+
0+
2610 4+
1780 2+
1100 2+
0+
Theory
Experiment
44Ar

Fig. 1.1 Comparison of the excited states in ^{44}Ar from the theoretical calculations of Retamosa *et al* [14] and the experimentally observed levels of S. Wan *et al* [15].

B. Fornal *et al.* [16] in looking for new states in ^{44,46}Ar isotopes using a deep-inelastic ion reactions, observed an energy level at 1158 keV for the 2_1^+ state, and a higher level at 2746 keV for a 4^+ state. Both studies [15,16] concluded that the N=28 closure persists even if a large neutron excess exists. In addition, H. Sheit *et al.* [17] in an experiment using proton scattering on ^{42,44}Ar extracted quadruple deformation parameter values of $|\beta_2| = 0.32 \pm 0.05$ for the 2_1^+ in ^{42}Ar and $|\beta_2| = 0.31 \pm 0.05$ for the same state in ^{44}Ar. H. Sheit *et al.*, in the same experiment, observed an energy of 1167 ± 40 keV for the 2_1^+ state, in comparison to an energy of 1144 ± 17 keV for the same state in an earlier experiment using Coulomb excitation [6].

This work, "The β^- Decay of ^{44}Cl", is based on an experiment conducted at the NSCL as a continuation of a series of experiments to study the structure in the region near N=28. Persuaded by the fact that the projectile fragmentation beams have made it possible to reach this region, the aim of this work is to study the structure of ^{44}Ar. With N=26 for ^{44}Ar, the goal is to check whether its structure looks like the vibrational structure of ^{42}Ar, with N=24, or the shell model structure of ^{46}Ar, with N=28. In this work the energy level scheme of ^{44}Ar and the half-life of ^{44}Cl, produced via fragmentation of an 80 MeV/nucleon ^{48}Ca beam in the A1200 fragment separator of the NSCL, will be presented.

CHAPTER II

THEORETICAL BACKGROUND

The need for a simple view of the nucleus, as indicated by Krane [18], arises from the very fact that it is a complex system. The complexity of the nucleus appears not only in the uncertainty of the nature of the interactions between its constituents, nucleon-nucleon interactions, but also in the large number of these interactions. This simple view, called a model, is needed to help make calculations, which makes it easier to understand nuclear structure.

2.1 The Shell Model

2.1.1 Shell Model Potential

The prediction that nucleons, protons and neutrons (fermions), are ordered in shells follows from the Pauli Exclusion Principle, which states that no two fermions, protons or neutrons, can co-exist in the same state and have the same sets of quantum numbers. Experimental data confirmed that nuclei with certain numbers of neutrons or protons are particularly stable. These numbers, called magic numbers, are 2, 8, 20, 28, 50, 82, and 126 [1,2,18].

The principal assumption of the shell model is that the potential created by all other nucleons (neutrons or protons) determines the motion of any nucleon. The energy levels are obtained by solving the three dimensional Schrödinger equation by implementing two potentials: the infinite square well and the harmonic oscillator potentials [18].

As in the case of electrons, the Pauli exclusion principle demands that no more than $2(2l+1)$ nucleons of a kind can occupy a level of a given orbital with angular momentum l. Spectroscopic notation (n l) is used to label the levels. The Principle quantum number, n, indicates the number of the level with that l value. So, the 1s state, with $l = 0$, indicates the lowest level which has room for two protons and two neutrons. The next state is 1p, where $l = 1$, with a maximum of 6 identical nucleons so that, together with the 1s state, there is room for 8 nucleons of one kind. Magic numbers at 2, 8, and 20 are easily reproduced with these potentials, but the others at 28, 50, 82, and 126 are not. Modifications were made to the infinite square well potential to rectify its erroneous assumptions of an infinite nucleon (neutron or proton) separation energy, and its sharp edges. Again, magic numbers beyond 2, 8, and 20 are not successfully reproduced. To obtain the proper magic numbers, an additional potential, the spin-orbit potential, must be considered [18].

2.1.2 Spin-Orbit Coupling

Scattering experiments, where an incident beam of nucleons is scattered by a target of nucleons, have shown strong evidence for the existence of the nucleon-nucleon spin-orbit force [18]. In the late 1940's [18], Haxel, Jensen, and Suess were able to show that including a spin-orbit term in the potential could give the subshells the proper separation. The total angular momentum is, as in atomic physics, given by $j = l + s$, with $s = \pm 1/2$ for a single nucleon. Therefore the possible values for the total angular momentum are $j = \ell + 1/2$ and $j = \ell - 1/2$. (For $l = 0$ only the $j = 1/2$ value is allowed). For the 1g level, $\ell = 4$, the degeneracy is $2(2\ell+1) = 18$, with j values of $7/2$ or $9/2$ (since $j = \ell \pm 1/2$). Therefore we will have $1g_{7/2}$ with room for 8 and $1g_{9/2}$ with a room of 10 states. There is an energy separation of these spin-orbit pairs (e.g., $1g_{7/2}$ and $1g_{9/2}$) that is proportional to the expectation value of $\vec{\ell} \bullet \vec{s}$ for each state. Since the $\vec{\ell} \bullet \vec{s}$ expectation value is given by

$$\langle \vec{\ell} \bullet \vec{s} \rangle = 1/2[j(j+1) - \ell(\ell+1) - s(s+1)]\hbar^2 \qquad (2.1)$$

The energy difference of any pair is given by

$$\langle \vec{\ell} \bullet \vec{s} \rangle_{j=\ell+1/2} - \langle \vec{\ell} \bullet \vec{s} \rangle_{j=\ell-1/2} = 1/2(2\ell+1)\hbar^2 \qquad (2.2)$$

This shows that the energy gap between the pair increases as ℓ increases [18]. Since equation (2.1) is positive for $j = \ell + 1/2$ and negative for $j = \ell - 1/2$, the energy level is lowered for the nucleons in the $j = \ell + 1/2$ state and raised for nucleons in the $j = \ell - 1/2$ state when we choose the $V(r)$ part of the spin-orbit interaction $V(r)\vec{\ell} \bullet \vec{s}$ term to be negative. Fig. 2.1 shows the energy levels in the shell-theory potential.

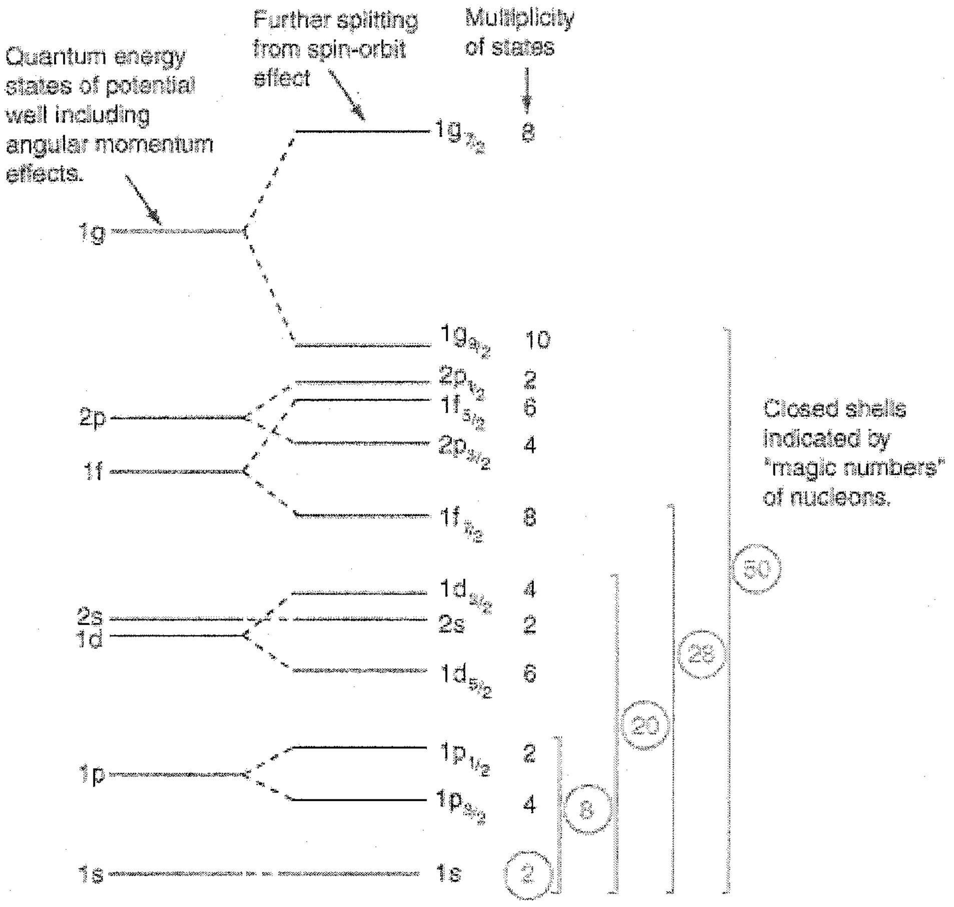
Quantum energy states of potential well including angular momentum effects.
Further splitting from spin-orbit effect
Multiplicity of states
1g
2p
1f
2s
1d
1p
1s
$1g_{7/2}$ 8
$1g_{9/2}$ 10
$2p_{1/2}$ 2
$1f_{5/2}$ 6
$2p_{3/2}$ 4
$1f_{7/2}$ 8
$1d_{3/2}$ 4
2s 2
$1d_{5/2}$ 6
$1p_{1/2}$ 2
$1p_{3/2}$ 4
1s ②
⑧
⑳
(28)
㊿
Closed shells indicated by "magic numbers" of nucleons.

Fig. 2.1 Single Particle energy levels showing the splitting due to the spin-orbit effect [19].

2.1.3 Excited States

Excited states are formed by promoting one or more nucleons into higher energy orbits. The extreme independent particle model assumes that all nucleons are paired except one, which determines the nuclear properties of a certain nuclide. For example, according to this model the excited states of ${}^{43}_{20}Ca_{23}$ are determined solely by the 23rd neutron. However, an accurate approach should consider all of the valance nucleons; the three neutrons in this case [18].

The formation of excited states in even "A" mass number nuclides is more complicated and can be attained in many ways. To form excited states, one excites nucleons to higher-lying orbital or breaks pairs to recouple at higher spins. The spin and parity of the levels are determined by the coupling between the two odd nucleons. Considering ${}^{44}_{18}Ar_{26}$, it has a $\pi(1d_{3/2})^2\ \nu(1f_{7/2})^6$ configuration, with a 0^+ ground state as predicted by the shell model for all even-even nuclei [18]. One way of forming an excited state for ${}^{44}_{18}Ar_{26}$ is by breaking an $s_{1/2}$ pair and exciting one of the two $s_{1/2}$ neutrons to the $f_{7/2}$ subshell. The result of coupling the $s_{1/2}$ neutron with the unpaired $f_{7/2}$ neutron will give a total angular momentum ranging from $7/2-1/2=3$ to $7/2+1/2=4$, with odd parity states. Another way would be for the two $s_{1/2}$ neutrons to be excited to fill the $f_{7/2}$ subshell, then excite one of the $d_{3/2}$ neutrons to the $s_{1/2}$ subshell. The odd neutron in each of the $s_{1/2}$ and $d_{3/2}$ subshells will couple to 1^+ or 2^+. Excited states can also be formed when one of the six neutrons from the $f_{7/2}$ subshell is excited to the $2p_{3/2}$ subshell. The subsequent properties are determined by coupling the unpaired neutrons in these two subshells. Coupling the angular momenta results in a $7/2-3/2=2$ to $7/2+3/2=5$ total angular momenta with even-parity states, namely $(2,3,4,5)^+$ states. It is obvious that different spin/parity combinations can be obtained by numerous combinations of nucleons in subshells. Actual states are composed of varying fractions of each possible state with the same spin and parity.

2.2 The Nilsson Model

Despite the fact that the spherical shell model has provided an excellent description of nuclei near closed shells, the compelling evidence for the existence of deformed nuclei necessitated a model that uses a deformed nuclear potential. This deformed single-particle potential with quadrupole deformation parameter β is the basis for the Nilsson (deformed shell) model. In the Nilsson model, orbitals are characterized by the asymptotic Nilsson quantum numbers that are represented by

$$K^{\pi}\left[N\, n_z \Lambda\right]$$

where K^{π} is the observed spin-parity of the state. K is then the projection of the total angular momentum, j, onto the symmetry axis, and π is the parity of the state, which is given by $(-1)^N$. The numbers in the bracket (the Nilsson quantum numbers) are: the principle quantum number (N), the number of nodes in the wave function along the symmetry axis Z (n_z), and the projection of the orbital angular momentum along the symmetry axis (Λ). (These will be discussed in detail later). The projection of the intrinsic nucleon spin onto the symmetry axis Σ ($=\pm 1/2$) is related to K, by definition, $K = \Lambda + \Sigma = \Lambda \pm 1/2$. Also, the possible values of n_z are according to the condition that the sum $n_z + \Lambda$ is even when N is even, and odd when N is odd [20].

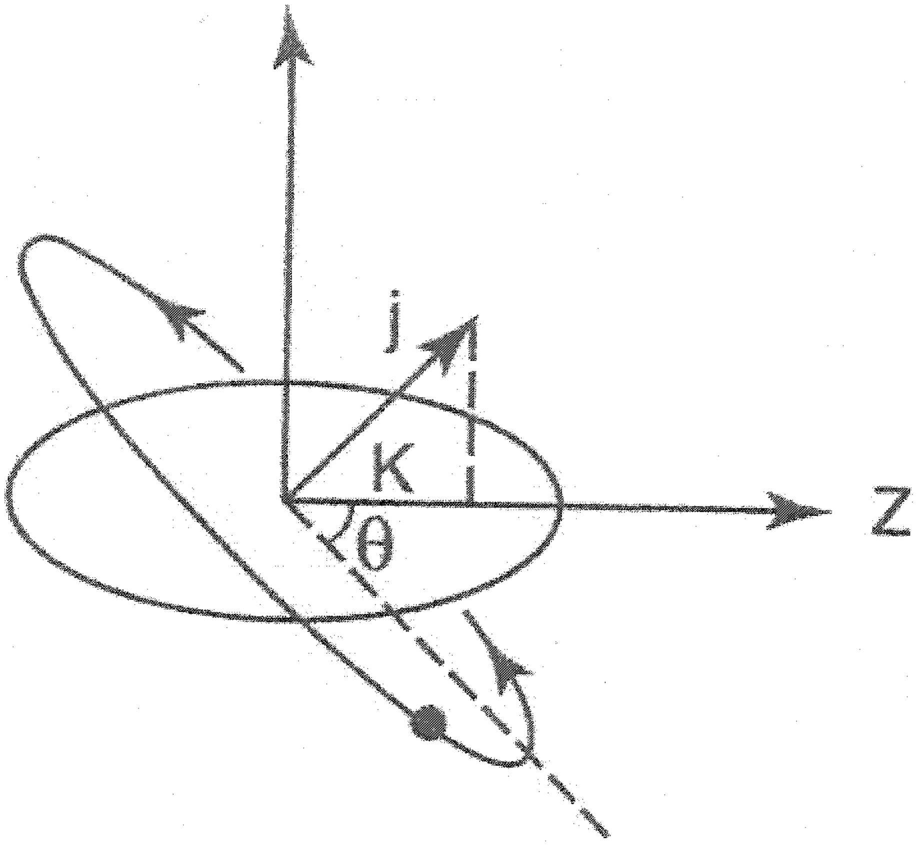

Fig. 2.2 Diagram showing the motion of a particle around a prolate deformed nucleus. Quantities j, K, and θ are discussed in the text [Casten, Ref. 20, page 333].

Consider the motion of a nucleon around a prolate deformed nucleus, i.e. one which is squeezed in two directions and extended along the Z direction , as shown in Fig 2.2. In the figure, the angle of the orbital plane, θ, can be defined as $\theta \approx \sin^{-1}(K/j)$. From the figure, it can be seen that for low K values (small θ) the motion is around and closer to a plane containing the Z axis of the nucleus and hence near the concentration of the nuclear matter. The interaction of the nucleon with the core results in a lowering of the energy. Also note that θ changes slowly with low K values and more rapidly for higher K, thus the difference in energy between successive K values increases as K increases. It is forbidden by the Pauli principle that any two levels with the same quantum numbers may cross, therefore when an orbit approaches another orbit with the same K and π, the two levels repel each other. Fig 2.3 shows the Nilsson diagram for the Z, N$\leq$ 50 region. Each line in the diagram represents a Nilsson state, whose rate of sloping upwards or downwards as a function of the deformation parameter depends on the angle of the orbit relative to the mass of the nucleus. Each line (state), as the Pauli principle requires, starts curving up or down as it approaches another line (state) with the same K and π. In its entirety, the structure of the diagram stands on three bases: the K splitting due to nuclear interaction in a deformed field, level-level splitting, and the input single-particle shell model [20].

The prescribed method for labeling of the Nilsson orbits is explained as follows. The first is to label the sequence of orbits starting from the same total angular momentum shell, i.e. a single particle orbital from the spherical shell model. Starting with the fact that the lowest lying orbits are those in which the wave function of the nucleon is most extended in the z direction. The wave functions of these orbits have the largest number of nodes along the z direction, and therefore the largest number of n_z. Hence, for a principle quantum number N, the maximum value n_z can take is n_z=N. For an orbit with a given N, the lowest energy orbit has a value $K = 1/2$. For example: a nucleon in the $f_{7/2}$ shell has N=3 and $\Lambda = 0$ or 1 because $K = \Lambda \pm 1/2$. Therefore the lowest N= 3 orbit is labeled as $K^{\pi}[N n_z \Lambda] \equiv 1/2^{-}[330]$. The next orbit from the $f_{7/2}$ shell has

$K = 3/2$, and n_z takes the next lower value; 2. Now, $\Lambda = K \pm 1/2$ implies $\Lambda = 1$ or 2, but the odd sum of $n_z + \Lambda$ requires $\Lambda = 1$. Therefore the Nilsson quantum numbers are $3/2^-[321]$. Following the same steps one can find the rest of the $f_{7/2}$ shell as $5/2^-[312]$, $7/2^-[303]$.

The Nilsson wave functions can be expressed as linear combinations of the wave functions of single-j shell model states and expansion coefficients C_j. For a deformed nucleus the Nilsson wave function is known as an intrinsic state or a state of excitation. A combination of this intrinsic motion and a superimposed rotational motion of the core makes up the real nuclear states. A nucleon in a particular Nilsson orbit in a deformed nucleus produces not just a single state, but a set of states comprising what is known as a rotational band [20].

The success of the Nilsson model in accounting for most of the features of single-particle levels of the deformed nuclei, qualifies it to be the first model referred to when new experimental information on such levels is obtained [20].

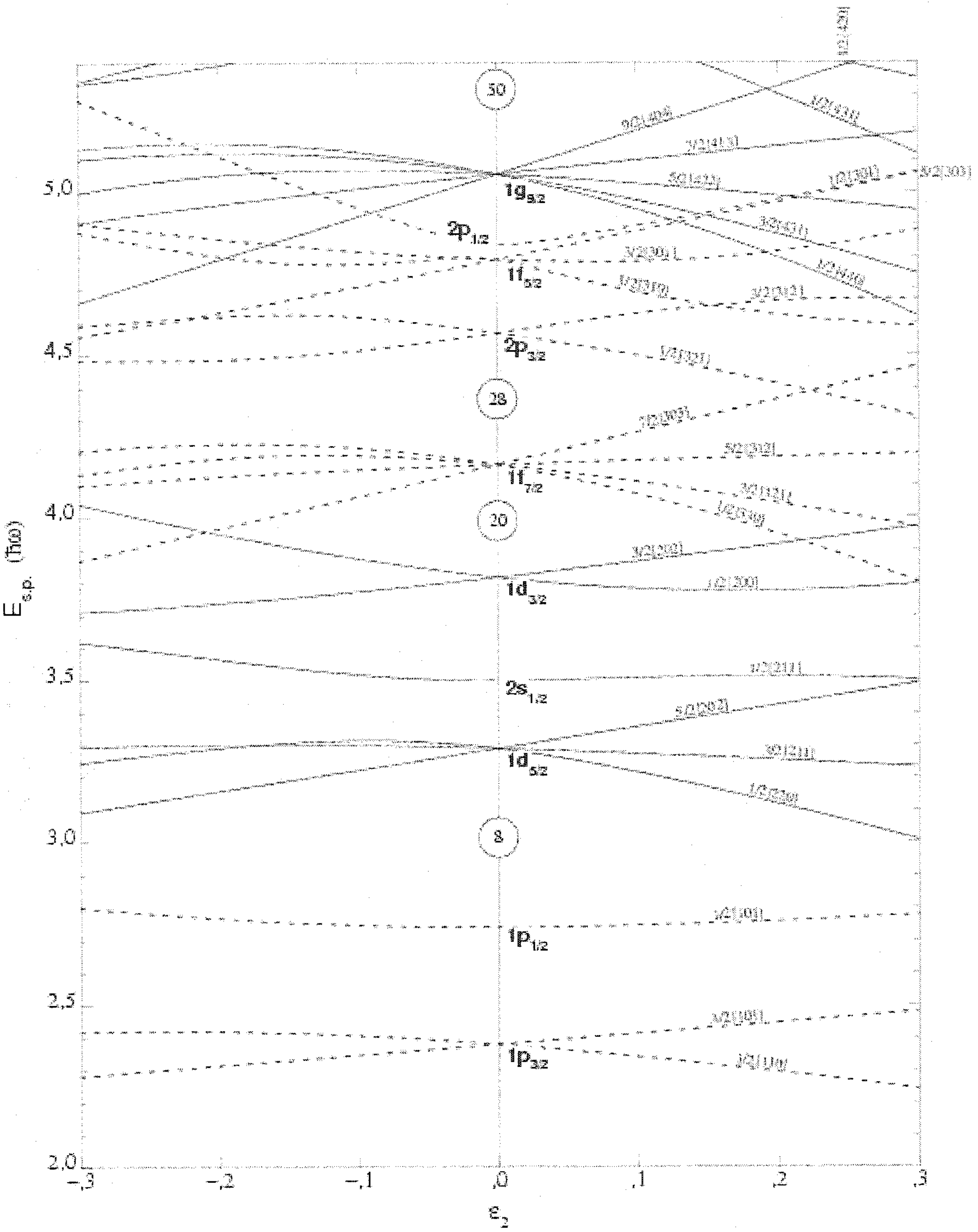

Fig.2.3 Nilsson diagram for Z, N$\leq$ 50 region. The deformation parameter $\varepsilon(\approx 0.95\beta)$ is the abscissa. The ordinate units, $\hbar\omega_0$, are given approximately by $41A^{1/3}$ MeV. [21]

2.3 The Collective Model

The collective model of the nucleus combines features of both the shell model (SM) and the Liquid Drop Model (LDM). The LDM is a simple model used to predict the shape and energy of the nucleus. In this model, the lowest energy state of the nucleus is the state with the lowest surface potential. Any change in the energy of the nucleus deforms the spherical shape (equilibrium state) of the nucleus [18].

The basic assumption of the collective model is that the nucleons in unfilled subshells move independently under the influence of a nuclear potential produced by the core of the filled subshells. Unlike the static spherically symmetrical potential of the shell model, here the potential undergoes deformation in shape. These deformations represent collective motion of the nucleons in the core that are associated with the liquid drop model [18]. In the following sections the two basic forms of motion in the collective model, vibrational and rotational, will be discussed in detail.

2.3.1 Vibrational Motion

The first form of the collective motion views the nucleus as being a liquid drop vibrating at high frequency. Despite the fact that the average shape of the nucleus is spherical, the instantaneous shape is not. A point on the nuclear surface at (θ,ϕ) is given by the instantaneous coordinate R(t) [18], which is expressed as an expansion of spherical harmonics $Y_{\lambda\mu}(\theta,\phi)$ with a time-dependant amplitude $\alpha_{\lambda\mu}$ (t):

$$R(t) = R_{av} + \sum_{\lambda\geq 1}\sum_{\mu=-\lambda}^{+\lambda} \alpha_{\lambda\mu}(t)\, Y_{\lambda\mu}(\theta,\phi) \qquad (2.3)$$

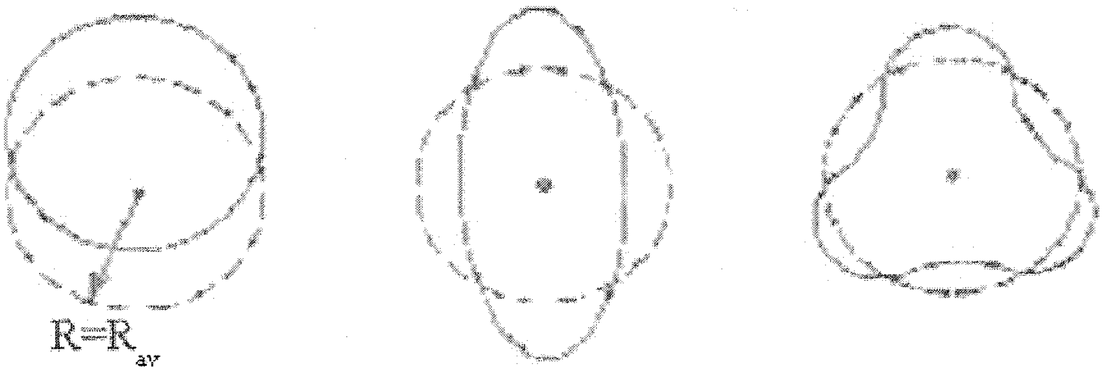

$\lambda = 1$ (*Dipole*) $\lambda = 2$ (*Quadrupole*) $\lambda = 3$ (*Octupole*)

Fig. 2.4 The first three vibrational modes of a nucleus. Solid lines show the view of the vibrating surface, where as the dashed lines the spherical equilibrium of the nucleus. Figure taken from Krane [Ref. 18, page 140].

Reflection symmetry necessitates, since $\alpha_{\lambda\mu}$ is not entirely random, that $\alpha_{\lambda\mu} = \alpha_{\lambda-\mu}$. The average radius is taken to be $R_{av} = R_0 A^{1/3}$, into which the constant $\lambda = 0$ is incorporated. A dipole vibration occurs when $\lambda = 1$, as shown in Fig. 2.4. The displacement of the center of mass indicates that this mode cannot due to the internal nuclear force.

The quadrupole vibration, the next lowest mode, occurs when $\lambda = 2$. In analogy to a photon as a unit of electromagnetic energy in quantum theory, a quantum of vibrational energy is called a phonon. Therefore a quadrupole phonon, when $\lambda = 2$, is a single unit of vibrational energy.

When one unit of vibrational energy is added to the 0^+ ground state of an even-even nucleus, the angular momentum increases by 2 units, because the phonon, $\lambda = 2$, carries 2 units of angular momentum. This results in a 2^+ state since the parity of $Y_{\ell m}$ is $(-1)^\ell$.

In adding a second quadrupole phonon, one must consider the 5 components of μ (2, 1, 0, -1, -2) for each phonon. This results in 25 combinations of the λ_μ for the two phonons. From these 25 combinations the total spin values must be extracted. The one of combination that will give $\mu_{tot} = 4$ is (2, +2). The number of combinations that will give $\mu_{tot} = 3$ are two: {(1, 2) and (2,1)}; but for the symmetry of the wave function of the phonon with integer spin, these two must be combined into one state. For $\mu_{tot} = 2$ we will have (2,0), (0,2), (1,1), where again the symmetric wave function necessitates the first two be combined, and therefore we will have only two combinations; [(2,0), (0,2)] and (1,1). For $\mu_{tot} =1$, we will have two combinations; [(2,-1), (-2,1)] and [(1,0), (0,1)]. For $\mu_{tot} = 0$, we will have three combinations; (0,0), [(1, -1), (-1,1)] and [(2, -2), (-2,2)]. For $\mu_{tot} = -1$, we will have two combinations; [(1,-2), (2,1)] and [(0, -1), (-1,0)]. For $\mu_{tot} = -2$, we will have two combinations; [(0, -2), (-2,0)] and (-1, -1). For $\mu_{tot} = -3$, we will have one combination; [(-1, -2), (-2, -1)]. And finally there will be one combination for $\mu_{tot} = -4$, (-2, -2) [18]. Therefore we will have 15 allowed combinations instead of 25, and these combinations can be grouped as follows:

$j = 4 \quad \mu_{tot} = +4, +3, +2, +1, 0, -1, -2, -3, -4$

$j = 2 \quad \mu_{tot} = +2, +1, 0, -1, -2$

$j = 0 \quad \mu_{tot} = 0$

Therefore, since two phonons carry twice the energy of a single phonon, a triplet of states with spins 0^+, 2^+, 4^+ is expected at twice the energy of the 2_1^+ state. Following similar arguments, a quintuplet of states with spins 0^+, 2^+, 3^+, 4^+, 6^+ is expected for three phonons at three times the energy of the 2_1^+ state [18].

The octupole mode, $\lambda = 3$, which carries three units of angular momentum and negative parity is the next highest mode of vibration. At energies above the two- phonon state a 3^- state is expected when a single octupole phonon is added to the 0^+ state [18].

Experiments have confirmed many of the predictions of the vibrational model. One of these predictions is that the ratio of the energy of the 4_1^+ member of a two-phonon triplet will be at twice the energy of the 2_1^+ state [20]. However, experiments have indicated that the average energy of the two phonon states is slightly greater than twice that of the energy of the one phonon state (typically, $E_{2ph}/E_{1ph} \sim 2.2$). The anharmonicity of the potential, due to the increasing number of the valance nucleons, causes the breaking of the degeneracy of the two phonon states. In essence, the potential change, as the result of the increasing number of the valence nucleons, leads to anharmonicities of the energy levels. These anharmonicities are manifested in that the energy will not be exactly n-times the one phonon energy, the degeneracy in multi-phonon multiplets will be broken, and the de-excitation transition will not necessarily follow the phonon model selection rule: $\Delta N_{ph} = \pm 1$, where N_{ph} is the number of phonons [20].

2.3.2 Deformed Nuclei

The nuclear surface can be characterized by giving its radius R as mentioned previously. For nuclei with quadrupole distortions, the radius R can be written as

$$R = R_0\left(1+\sum_{\mu}\alpha_\mu \mathrm{Y}_{2\mu}(\theta,\phi)\right) \quad (2.4)$$

where R_0 is the radius of the spherical nucleus, $\mathrm{Y}_{2\mu}(\theta,\phi)$ are the spherical harmonics of order two, and the quantities α_μ ($\mu = 0, \pm 1, \pm 2$) are called deformation parameters [20]. When $\alpha_\mu = 0$, the nucleus is said to be spherical while it said to be deformed when $\alpha_\mu \neq 0$. The nuclear shape can be specified by writing the five α_μ in terms of two intrinsic variables β and γ as follows:

$$\left.\begin{aligned} &\alpha_0 = \beta\cos\gamma \\ &\alpha_2 = \alpha_{-2} = \frac{1}{\sqrt{2}}\beta\sin\gamma \\ &\alpha_1 = \alpha_{-1} = 0 \end{aligned}\right\} \quad (2.5)$$

where β gives the quadrupole deformation extent, whereas γ gives the axial asymmetry degree. In their ground state, most nuclei are at or close to being axially symmetric, and the potential has a minimum at $\gamma = 0$. The Lund convention of β and γ for an axially symmetric prolate nucleus is $\beta > 0$ and $\gamma = 0^0$, whereas for an axially oblate nucleus $\beta > 0$ and $\gamma = 60^0$. An alternate convention has the value of γ ranging from 0^0 to 30^0 corresponding to axially symmetric to maximum axial symmetric, with $\beta > 0$ for prolate nuclei and $\beta < 0$ for oblate nuclei [20]. Fig 2.5 shows types of nuclear deformations.

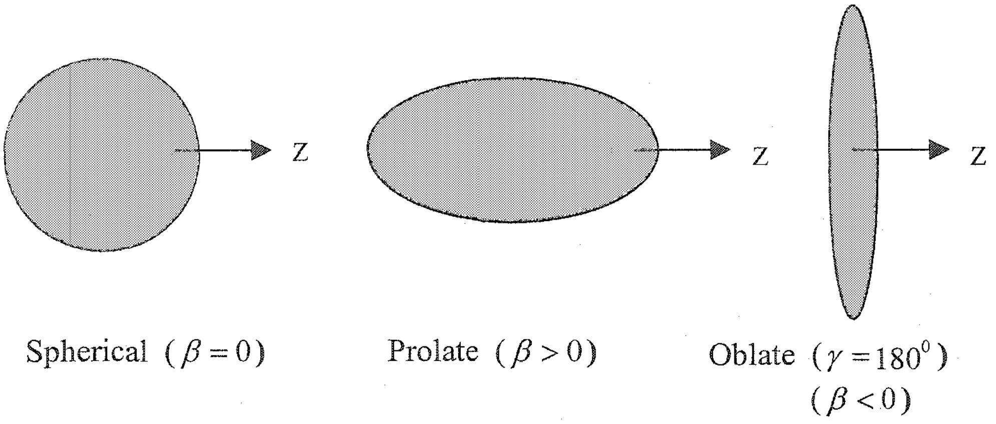

Fig. 2.5 Schematic diagram showing how nuclear deformations depend on the value of β. Arrows indicate the symmetry axis [Casten [20] page 198].

Very few nuclei have spherical shapes in their ground states and different shapes can be observed within the same nucleus. Despite the fact that spherical shapes dominate near closed shells, the large number of valence nucleons between closed shells leads to nuclear deformations [20].

A quadrupole-deformed nucleus can be described by two quantities: the moment of inertia, I, and the quadrupole moment, $Q(\beta)$. The values of the quadrupole moment are positive for the nucleons of the j orbits early in the major shell. However, the contribution to the quadrupole moment value decreases as the shell fills, vanishes and becomes negative at the end of the shell [2,18,20]. The intrinsic quadrupole moment Q_0 is given by

$$Q_0 = \frac{3}{\sqrt{5\pi}} Z R_0^2 \beta(1 + 0.16\beta) \qquad (2.6)$$

where Z is the proton number and $R_0$is the radius of the spherical nucleus. Typically, $\beta \approx 0.3$ for an actual deformed nucleus, whereas, for super-deformed nuclei β has a value close to 0.6.

2.3.3 Rotational Motion

Rotational motion is the most evident characteristic of the non-spherical or deformed nuclei. These rotations occur about an axis perpendicular to the symmetry axis. The quadruple moment of these nuclei are found to be unexpectedly high, indicating a large nuclear deformation [2, 18, 20]. When the nucleus rotates at angular frequency ω, it carries an angular momentum of $I\omega$, where I is the moment of inertia, and the energy is given by

$$E = \frac{\hbar^2}{2I}\ell(\ell+1) \qquad (2.7)$$

where ℓ is the angular momentum quantum number which takes values of 0, 2, 4, etc. [18, 20]. Therefore, the expected energies of the rotational band of states are

$$\left.\begin{aligned} E(0^+) &= 0 \\ E(2^+) &= 6(\tfrac{\hbar^2}{2\mathrm{I}}) \\ E(4^+) &= 20(\tfrac{\hbar^2}{2\mathrm{I}}) \\ E(6^+) &= 42(\tfrac{\hbar^2}{2\mathrm{I}}) \end{aligned}\right\} \qquad (2.8)$$

For a rotational band built on a 0^+ ground state, the ratio $E(4^+)/E(2^+) = 3.33$ is one of the important signatures for the rotational motion and deformation [18,20].

The energy spacing within bands for two successive energies differing by two units of angular momentum ($\Delta\ell = 2$) indicates that the γ ray transitions between members of a band are always E2. Using equation (2.7);

$$E(\ell \to \ell-2) \equiv E(\ell) - E(\ell-2) = \frac{\hbar^2}{2I}[\ell(\ell+1) - (\ell-1)(\ell-2)]$$

$$= \frac{\hbar^2}{2I}(4\ell - 2) \qquad (2.9)$$

If we substitute $\ell = 2,4,6,8$ in equation (2.6), we get; $6(\frac{\hbar^2}{2\mathrm{I}})$, $14(\frac{\hbar^2}{2\mathrm{I}})$, $22(\frac{\hbar^2}{2\mathrm{I}})$, $30(\frac{\hbar^2}{2\mathrm{I}})$, respectively. γ-ray spectra from these transitions exhibits uniformly spaced peaks separated by $8(\frac{\hbar^2}{2\mathrm{I}})$, called a "picket fence", and are one of the best experimental signatures of a rotational band [20].

2.4 Understanding ^{44}Ar

In the early studies of the ^{44}Ar nuclide, G. M Crawley *et al* [10], using the reaction ^{48}Ca(^{3}He, ^{7}Be) ^{44}Ar, observed the excited states: 0.75 ± 0.03 MeV, 1.61 ± 0.03 MeV, 3.48 ± 0.03 MeV, 3.98 ± 0.05 MeV, and 4.43 ± 0.04 MeV. Using intermediate energy Coulomb excitation, H. Sheit *et al.* [6] measured the 2_1^+ state in ^{44}Ar at 1144 ± 17 keV. In their shell model study of the neutron–rich nuclei around N=28, Retamosa *et al.* [14] investigated the effect of the large neutron excess on the N=28 shell gap. Calculations predicted the low-lying 2^+ first excitation energy state at 1182 keV for ^{44}Ar. S. Wan *et al.* [15], as shown in Fig. 1.1, measured the states 2_1^+, 2_2^+ and 4_1^+ at 1100 keV, 1780 keV and 2610 keV respectively. B. Fornal *et al.* [16] in studying new states in ^{44,46}Ar isotopes using a deep-inelastic ion reaction, observed energy levels at 1158 keV, 2746 keV and 3439 keV for the 2_1^+, 4_1^+, and 6_1^+ excited states, respectively. H. Sheit *et al.* [17] in inelastic proton scattering measured the quadruple deformation parameters of $|\beta_2| = 0.32 \pm 0.05$ for the 2_1^+ in ^{42}Ar and $|\beta_2| = 0.31 \pm 0.05$ for the same state in ^{44}Ar.

In this report, with the aid of the previous studies and the various nuclear models, the structure of ^{44}Ar will be presented. The energy levels, their ratios, as well as the spin/parity will be used to understand the structure of ^{44}Ar. As will be shown in detail in Chapter 5, this structure suggests the coexistence of both shell model and vibrational structure.

CHAPTER III

EXPERIMENTAL DETAILS

3.1 Introduction

Fragmentation of an 80 MeV/nucleon ^{48}Ca primary beam was used to produce a ^{44}Cl source by utilizing the A1200 fragment separator at the National Superconducting Cyclotron (NSCL). The ^{48}Ca primary beam was produced with the NSCL Room Temperature Electron Cyclotron Resonance (RTECR) ion source and accelerated through the K1200 cyclotron. Details of the production and separation of the ^{44}Cl source are described in the following sections.

3.2 Experimental Equipment

3.2.1 The K1200 Cyclotron

Although one of the earliest types of particle accelerator, the cyclotron is still used as a stand alone machine or as the first stage of some large multi-stage particle accelerators [22]. It makes use of the magnetic force on a charge moving in a magnetic field to bend moving charges into a semicircular path between accelerations by an applied electric field. The applied electric field oscillates to repeatedly accelerate ions between the dees of the magnetic field region. Constructed in 1990, the K1200 cyclotron is axially injected by one of three ECR ion sources: a two-stage room temperature ion source, a compact ion source, or a superconducting ECR ion source. With a magnetic field operating range of 3 to 5 T and a maximum magnetic rigidity of 5 T-m, the K1200 cyclotron is based on a 280 ton, 60 MJ superconducting magnet [22].

The non-relativistic relationship for the energies of magnetic-rigidity limited heavy–ion beams is given by:

$$E/A = K(Q/A)^2 \text{ MeV} \qquad (3.1)$$

where the K-value, the bending limit, for this machine is 1200 MeV. The maximum energies, for ions with Q/A greater than 0.33, are focusing limited and are given by:

$$E/A = K_f\,(Q/A) \text{ MeV} \qquad (3.2)$$

where K_f is 400 MeV. For radio frequencies from 9 to 27 MHz, the K1200 cyclotron is capable of accelerating light ions to over 200 MeV/nucleon, and heavy ions to over 50 MeV/nucleon [22].

3.2.2 Design and Characteristics of A1200 Fragment Separator

With its versatile operating modes, the A1200 serves as both a beam analyzing system for the K1200 cyclotron, as well as a projectile fragment separator for radioactive beam production. As a beam analyzing system, the A1200 was used to analyze primary beams that had been degraded in energy with degrader foils at the A1200 target location. As shown in Fig. 3.1, the A1200 connects the K1200 cyclotron with the transfer hall area where it can provide radioactive beams to any target location for secondary reaction studies or to the Reaction Product Mass Separator (RPMS) for additional separation. A water-cooled target was located at the OBJECT position for secondary beam production. The purity of secondary beams depends on the solid angle mode. The larger solid angle modes have lower resolving power and hence provide less purity. The target can be located anywhere between the OBJECT location to within 30 cm of the entrance of the first triplet. The lowest solid angle position is referred to as the medium acceptance mode while the largest solid angle position as the high acceptance mode [23].

3.2.3 The Reaction Product Mass Separator (RPMS)

The RPMS is a device that can be used to provide the additional filtering needed to produce ultra-pure radioactive beams. It can be used in combination with the A1200 to separate secondary beams or as a stand-alone separator. In the past, the RPMS has been used for decay studies far from stability [22]. In this experiment it was used only as a focusing beam line to transport the beam to the detecting system.

3.3 Reaction and Detector Set up

The 80 MeV/nucleon ^{48}Ca primary beam was produced using a metallic feed in a RTECR ion source and then accelerated in the K1200. The resulting beam had intensities ranging from 7 to 10 pnA.

Using a 376-mg/cm^2 ^{9}Be target, the ^{44}Cl fragments were produced and identified using standard energy loss versus time of flight techniques. The ^{44}Cl was observed at Bρ = 2.9073 Tm, as part of a cocktail beam after tuning the A1200 for maximum production of ^{41}P. For the initial selection of fragment ions, a 3% momentum slit was used at the

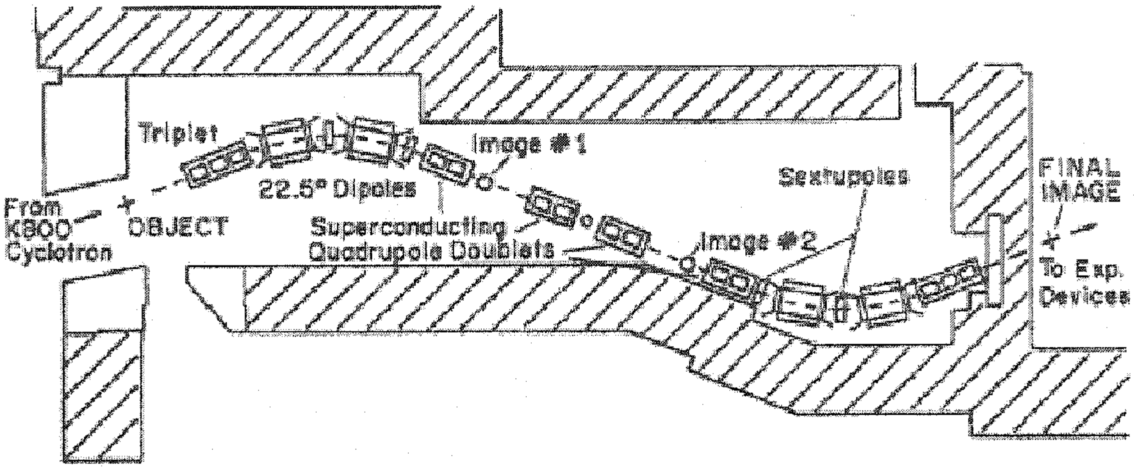
From K800 Cyclotron
OBJECT
Triplet
22.5° Dipoles
Image #1
Superconducting Quadrupole Doublets
Image #2
Sextupoles
FINAL IMAGE
To Exp. Devices

Fig. 3.1 Schematic layout of the A1200

first intermediate image (image #1 in Fig. 3.1) of the A1200. By using a thin plastic wedge placed at the second intermediate image (image #2 in Fig. 3.1), another separation of the fragment ions was obtained. The ions of ^{44}Cl, after passing through the wedge, were centered at the focal plane of the A1200 by tuning the second half of the device to 2.5300-T m rigidity.

A detector endstation was placed approximately 40 m downstream from the A1200 at the end of the RPMS. Ion beams separated at the end of the A1200 were transported to the detector endstation with an efficiency of about 65%. This resulted in an average beam intensity, at the detector endstation, of 140-430 ions per second of ^{44}Cl. Fig. 3.2 shows schematically the detector endstation used in this experiment.

A Si PIN diode detector located near the beam-line exit was used to measure energy loss (ΔE) of the ions before they were stopped in the rotating wheel. The time of flight (TOF) of the ions between a thin plastic scintillator placed at the A1200 exit and

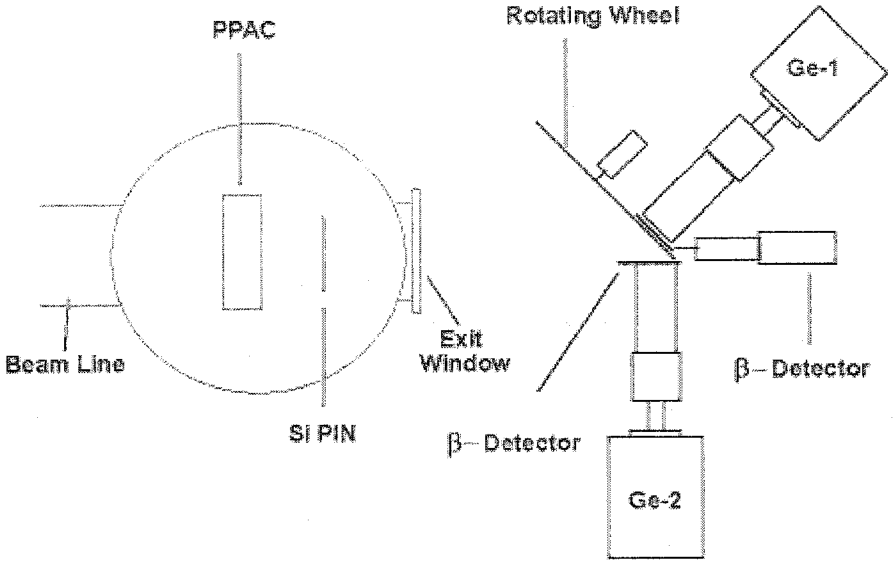

Fig. 3.2 Schematic layout of the detector endstation including particle tracking and identification detectors, rotating wheel into which the radioactive beam was implanted, two β detectors and two Ge detectors.

the Si PIN diode was measured. In addition, a parallel plate avalanche counter (PPAC) was used to monitor the beam position. Precise determination of the beam components was allowed by using these detectors. A plot of ΔE versus TOF is shown in Fig. 3.3. The idea of energy loss versus time flight for identifying particles is based on the quantum mechanical calculations of the collision process. Hans Bethe first introduced the calculation in 1930 [18]. In calculating the magnitude of the energy loss per unit length equation, Bethe showed that $\Delta E \propto v^{-2}$, where v is the velocity of the particle. Also, the product $\Delta E \cdot T$ is equal to $k Z^2 M$, where Z is the atomic number, and M is the mass of the particle to be identified. The graph of ΔE versus TOF shows a set of hyperbolas corresponds to different values of Z^2M. In Fig. 3.3 the hyperbolas show ^{44}Cl, ^{43}S, ^{42}S, and ^{41}P nuclei. (The limited momentum acceptance of the A1200 results in only seeing a small portion of each hyperbola.)

The ions exited the beam line through a 0.13 mm Kapton window, were energy degraded by a stack of Al foils, and were then embedded into 117 mg/cm^2 Al targets attached to a rotatable wheel oriented at 45^0 to the direction of the beam, providing an effective stopping thickness of ≈165 mg/cm^2. The wheel into which the separated ions were implanted consists of a 40 cm diameter wheel made from a 1/8-in-thick Al plate attached to a stepping motor. It had nine 5 cm diameter holes covered with the Al foils at a radius of 17.2 cm.

Identifying γ rays associated with a particular decay was achieved by not only different separator setting, but also by using different timing cycles. A typical timing cycle consisted of three steps. During the first step, the beam-on period, beam identification and decay data were collected as the beam was implanted into the wheel. By dephasing one dee of the K1200, the beam was turned off in the second step. Only data from the decay were collected during this step, the beam-off period. While the beam remained off during the third step, the wheel was stepped to a new position in approximately 300 ms. This allowed time for vibration to damp out before data collection was restarted. The large rotational inertia of the wheel and the maximum torque that could be achieved by the stepping motor extended the time for this movement step. Appendix A shows the programming code that operated the wheel's motor. Both sides of the wheel were shielded by a 3/8-in-thick steel plate to minimize the possibility

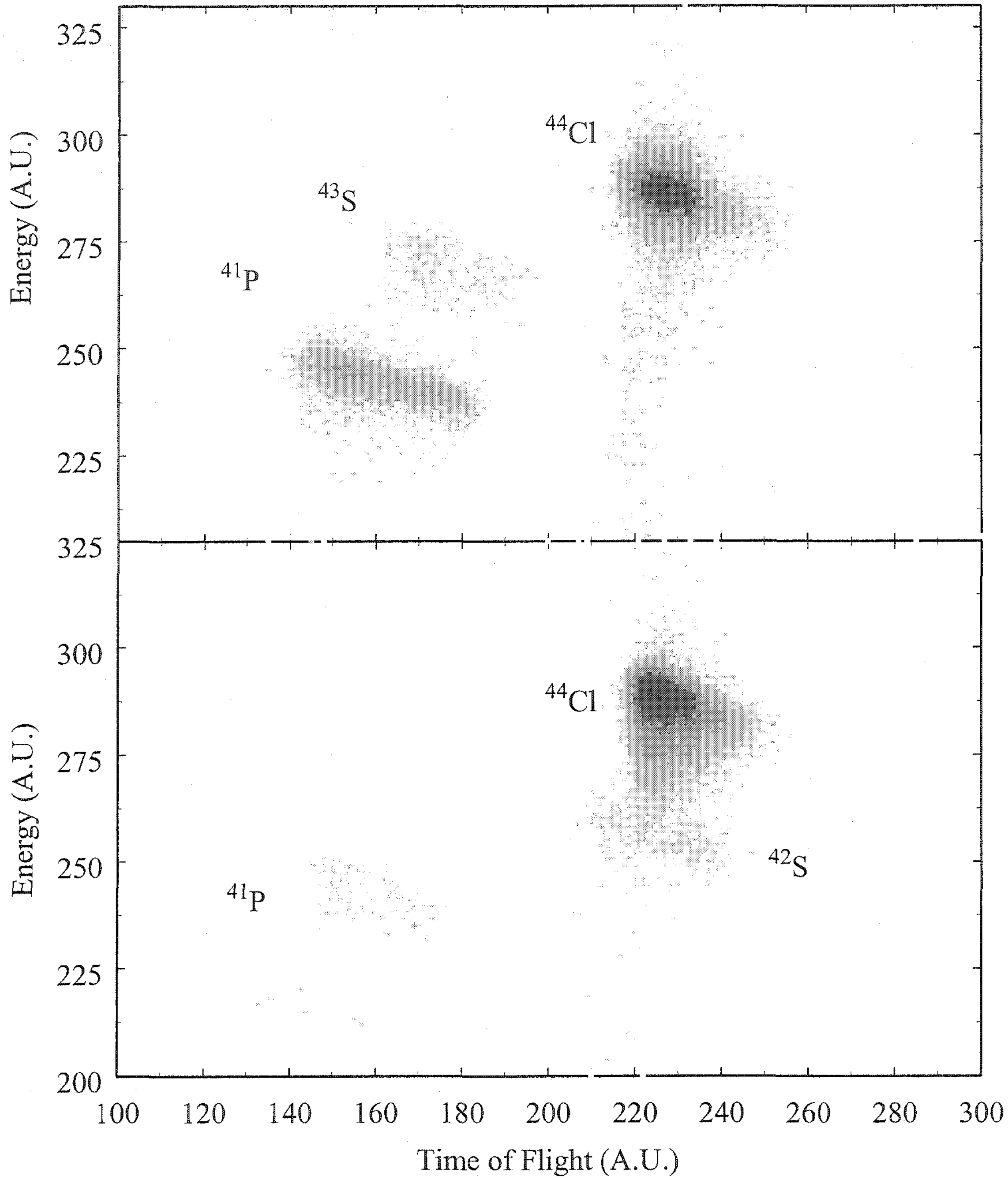

Fig. 3.2 Particle identification plots (ΔE versus TOF). The purity of the beam iscontrolled by the A1200 setting. The top shows the setting for ^{41}P, while bottom is that for ^{44}Cl. Small changes in the A1200 setting can result in very pure beams.

of γ-rays from a catcher foil other than the one at the beam position from reaching the germanium detectors.

Four detectors, two germanium detectors and two thin plastic scintillators, were used to observe the decays of the implanted ions. An 80% germanium detector, labeled Ge-1 in Fig. 3.2, was located behind the first β-detector with both being mounted in such a way that they made a 45^0 angle relative to the direction of the beam. A 120% germanium detector, labeled Ge-2, was placed in front of a second β-detector, with both mounted at a 90^0 angle relative to the direction of the beam. The Ge-1 and Ge-2 detectors were at distances of 1.2 cm and 5.7 cm, respectively, from the center of the implantation targets. From the four detectors, the timing signals were used to set hardware timing gates. Data were collected in two modes: beam events and decay events.

Beam events were collected whenever a particle triggered the Si PIN diode detector. This allowed continuous monitoring of the beam rate and purity as well as the total number of ions implanted. Decay events were taken any time a γ-ray was detected in one of the germanium detectors. This allowed collection of a γ-ray singles spectrum without any gating. By using the time correlation between detectors it was then possible to sort the data for the βγ, γγ, and βγγ coincidences. The time of each decay event in relation to the beginning of the decay cycle was recorded by resetting the clock for this measurement at the end of each cycle. This resulted in no time being recorded during the growth phase of the timing cycle. Data concerning energy and relative times were also recorded [7]. Appendix B shows the electronic set up of the experiment.

3.4 Energy and Efficiency Calibration

Standard sources of ^{60}Co, ^{88}Y, ^{152,154}Eu, and ^{125}Sb were used to do off-line calibration of the germanium detectors, whereas for the on-line calibration, known background lines were used. Because the standard sources provide an energy calibration only for energies ranging from 100 keV to 2.7 MeV, while γ-rays were observed at energies up to 5.4 MeV, a several-step process was used to obtain one consistent calibration. In the first step, the standard sources were placed at a distance from the detectors so that the detection rate was 100 cps, to limit any rate related gain shift. In the second step, the calibration, using the standard sources, was used to find the approximate energies of the background, β^+ annihilation and long-lived lines to check for the gain shifts between the run data and the calibration measurements. Significant gain shifts were observed indicating the need to develop an internally consistent calibration from the real source data. Hence the on-line data were used to establish revised calibration up to 2.6 MeV. In the third step, and in order to promote the calibration to higher energies, single and double escape peaks from the on-line radioactive sources were used.

Since it was possible that high-energy γ rays could be produced in the decay, given the large Q_β value, spectra were collected from each detector using two different gains. This allowed better histogramming resolution at low energies and the ability to observe high-energy (up to 8 MeV) γ rays. Figs. 3.4 through 3.7 show the low-energy, with a 0.5 keV/channel gain, and the high-energy, with a 1.0 keV/channel gain, spectrum calibrations for both detectors.

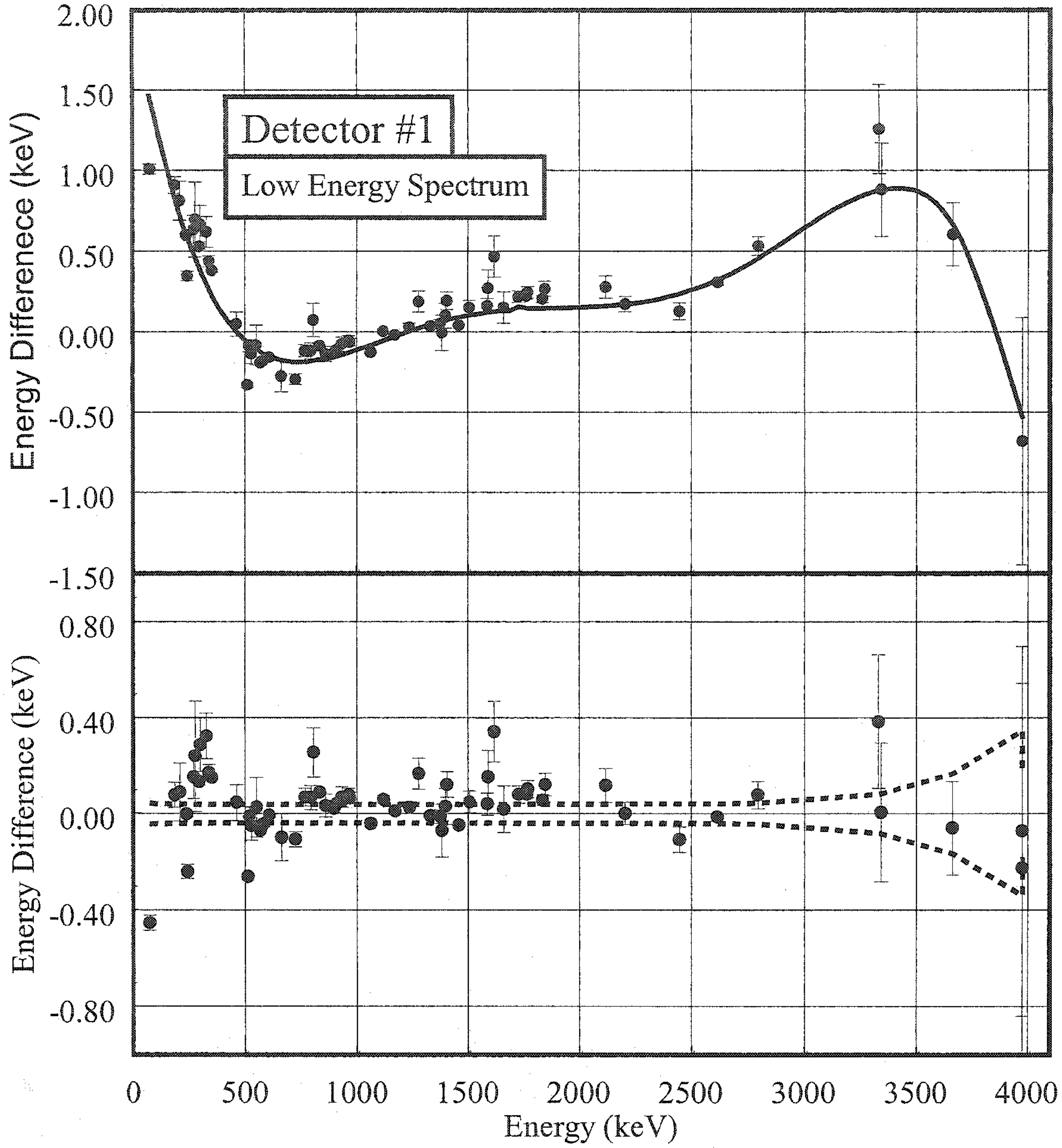

Fig 3.4 The low-energy calibration for the Ge-1 detector (gain≈ 0.5 keV/channel). The upper section shows the energy difference between the known energies and a linear fit to the data. The lower section shows the difference between the known energies and the final fit. The dashed lines indicate the limits (1σ) of the intrinsic uncertainty in the fit.

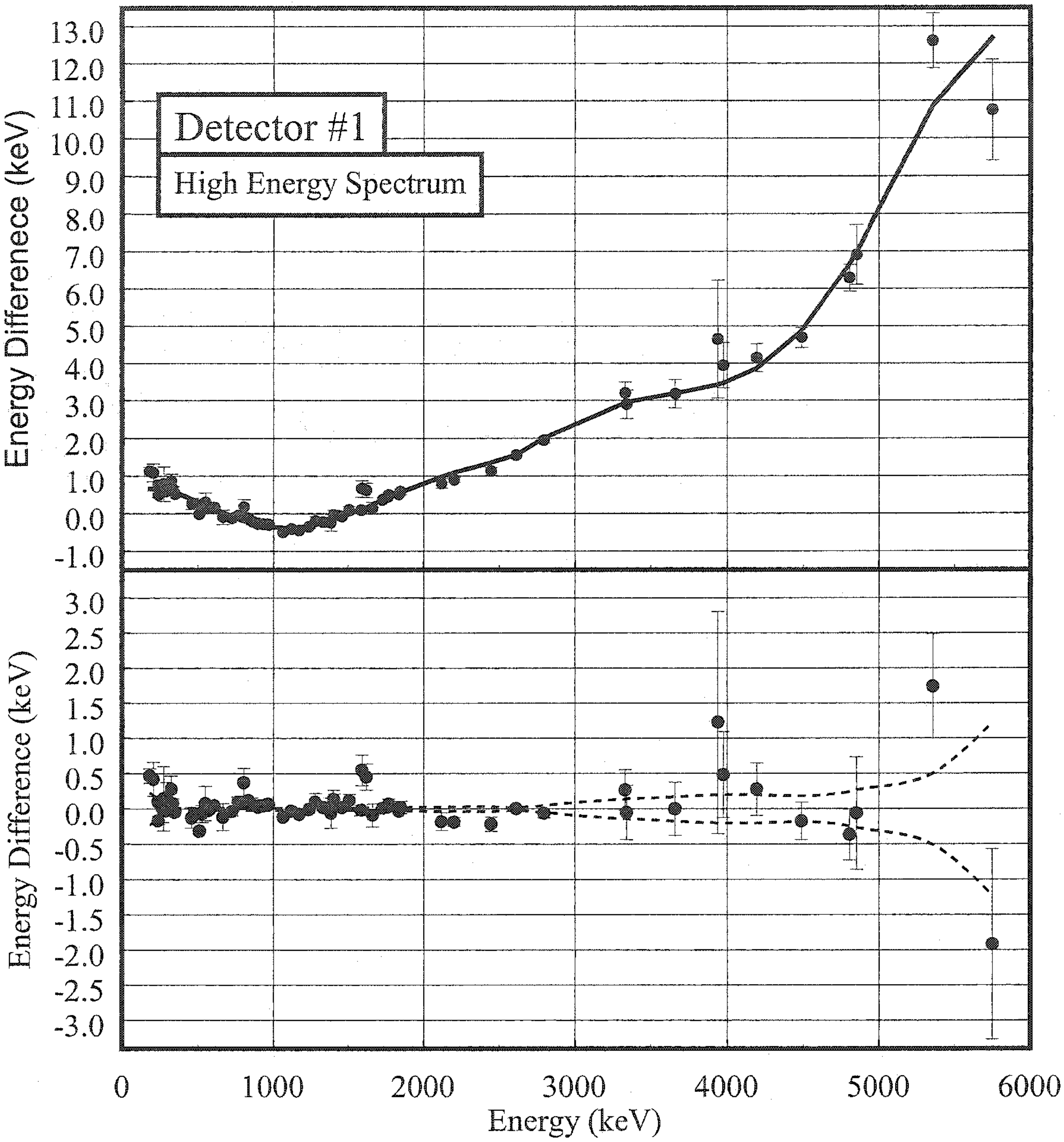

Fig 3.5 The high-energy calibration for the Ge-1 detector (gain$\approx$ 1.0 keV/channel). The upper section shows the energy difference between the known energies and a linear fit to the data. The lower section shows the difference between the known energies and the final fit. The dashed lines indicate the limits (1σ) of the intrinsic uncertainty in the fit.

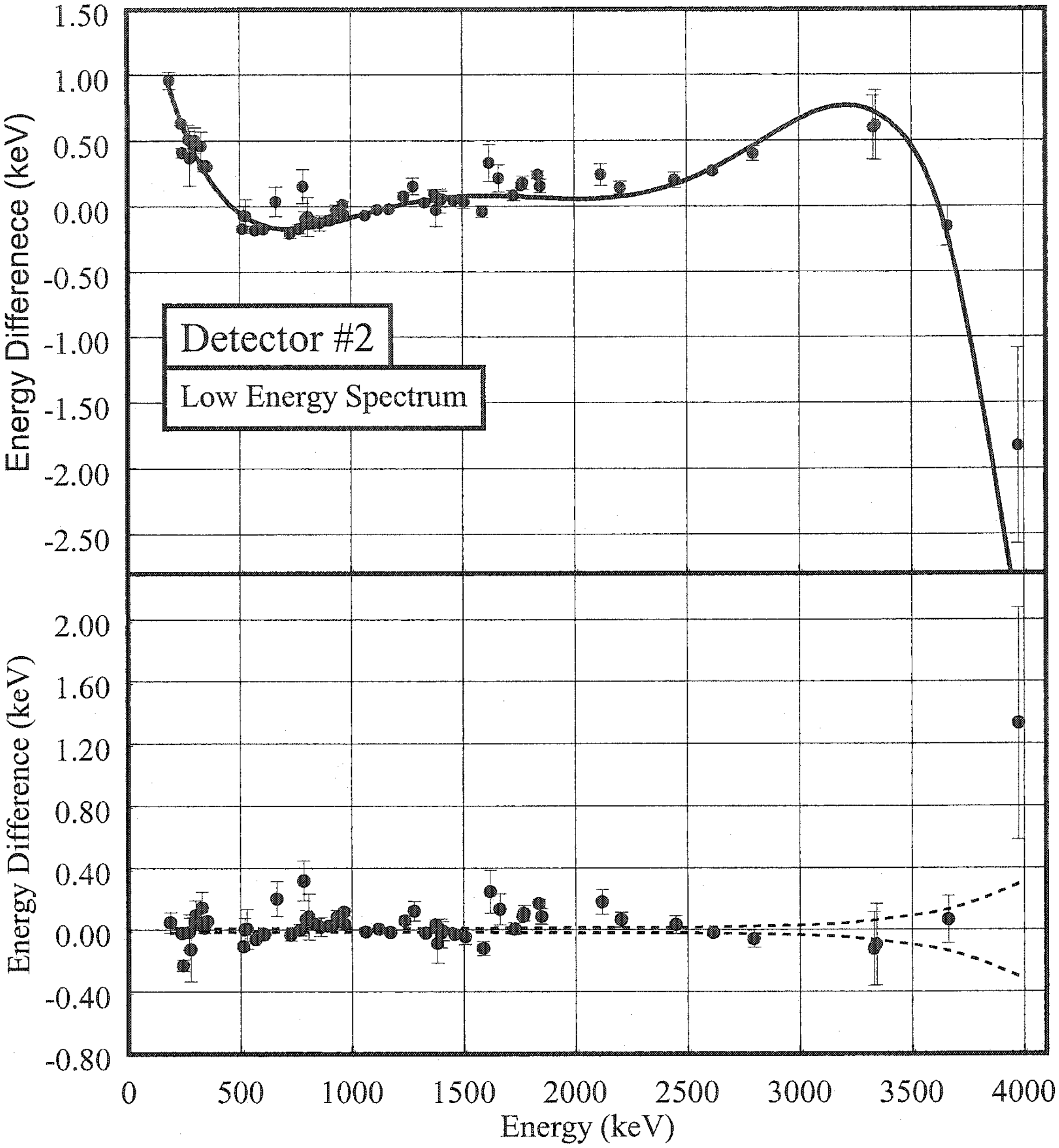

Fig 3.6 The low-energy calibration for the Ge-2 detector (gain≈ 0.5 keV/channel). The upper section shows the energy difference between the known energies and a linear fit to the data. The lower section shows the difference between the known energies and the final fit. The dashed lines indicate the limits (1σ) of the intrinsic uncertainty in the fit.

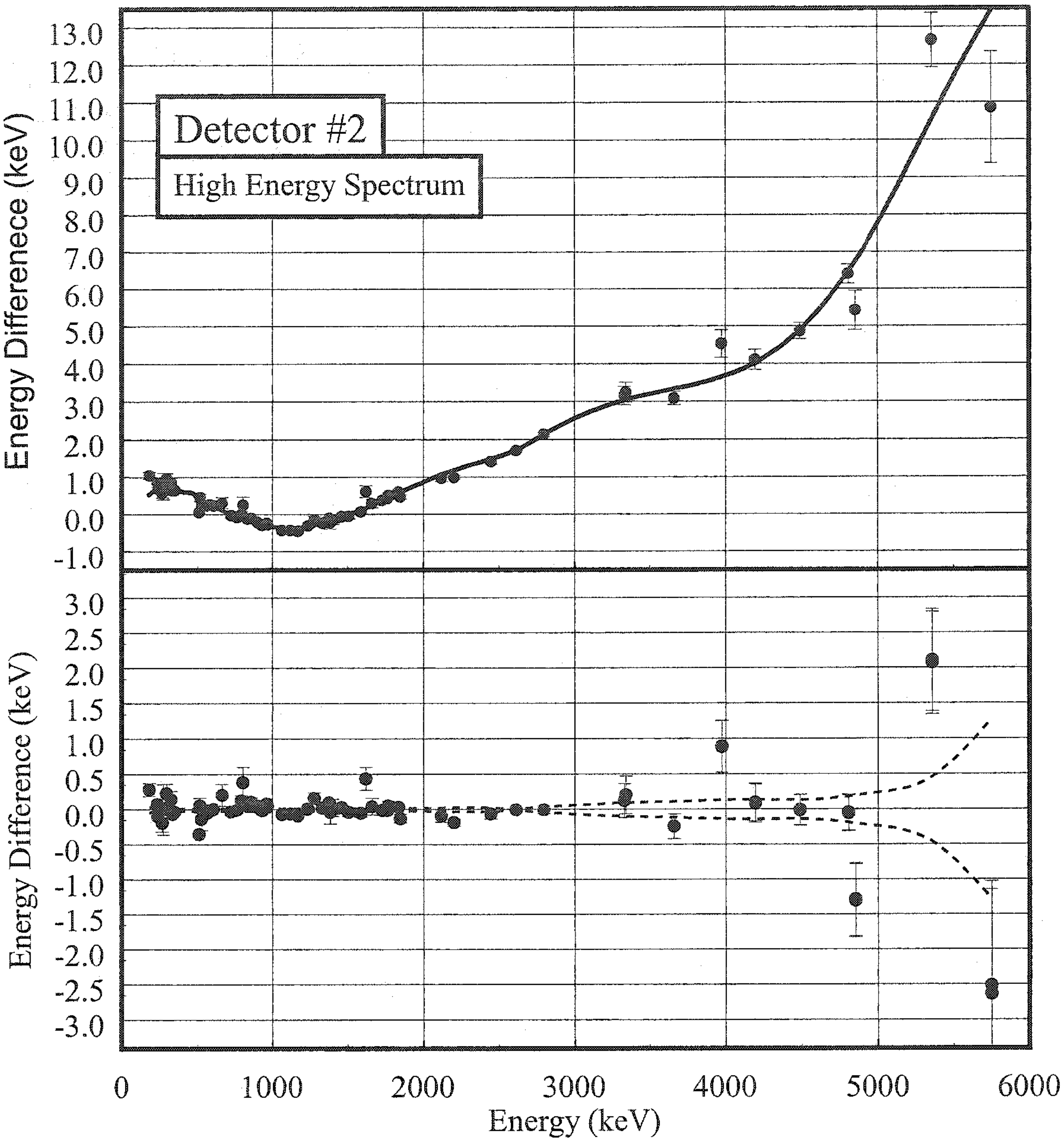

Fig 3.7 The high-energy calibration for the Ge-2 detector (gain≈ 1.0 keV/channel). The upper section shows the energy difference between the known energies and a linear fit to the data. The lower section shows the difference between the known energies and the final fit. The dashed lines indicate the limits (1σ) of the intrinsic uncertainty in the fit.

The efficiency calibration also required a multi-step process. Data were collected using the standard sources placed at the target position. This positioning was only approximate since they could not be placed inside a target and did not match the geometry of the actual beam. Theoretical efficiency curves were then calculated using the Monte Carlo Nuclear Physics (MCNP) program for both photopeak and total efficiency. These calculations were based on an assumed geometry for the beam spot and the known characteristics of the detectors. However, it did not take into account some of the absorbing materials present in the system. The ^{60}Co and ^{88}Y sum peaks were used to adjust the absolute normalization of the theoretical photopeak efficiency curves for each detector. The ^{152,154}Eu and ^{125}Sb data were then used to check the curves and to obtain a proper efficiency curve at energies below 200 keV. The theoretical curve was then assumed to be correct for the higher energies. A curve was fit to data points after a corrected set of absolute photopeak efficiencies was obtained [7]. Figs. 3.8 and 3.9 show the efficiency calibration spectra for the germanium detectors, each with upper and lower sections. The upper section, with error bars, shows the efficiency against the energy in a log-log plot. The solid line shows the photopeak efficiency and the dashed line shows the total efficiency curve. The lower section shows calibration uncertainty as a function of the energy

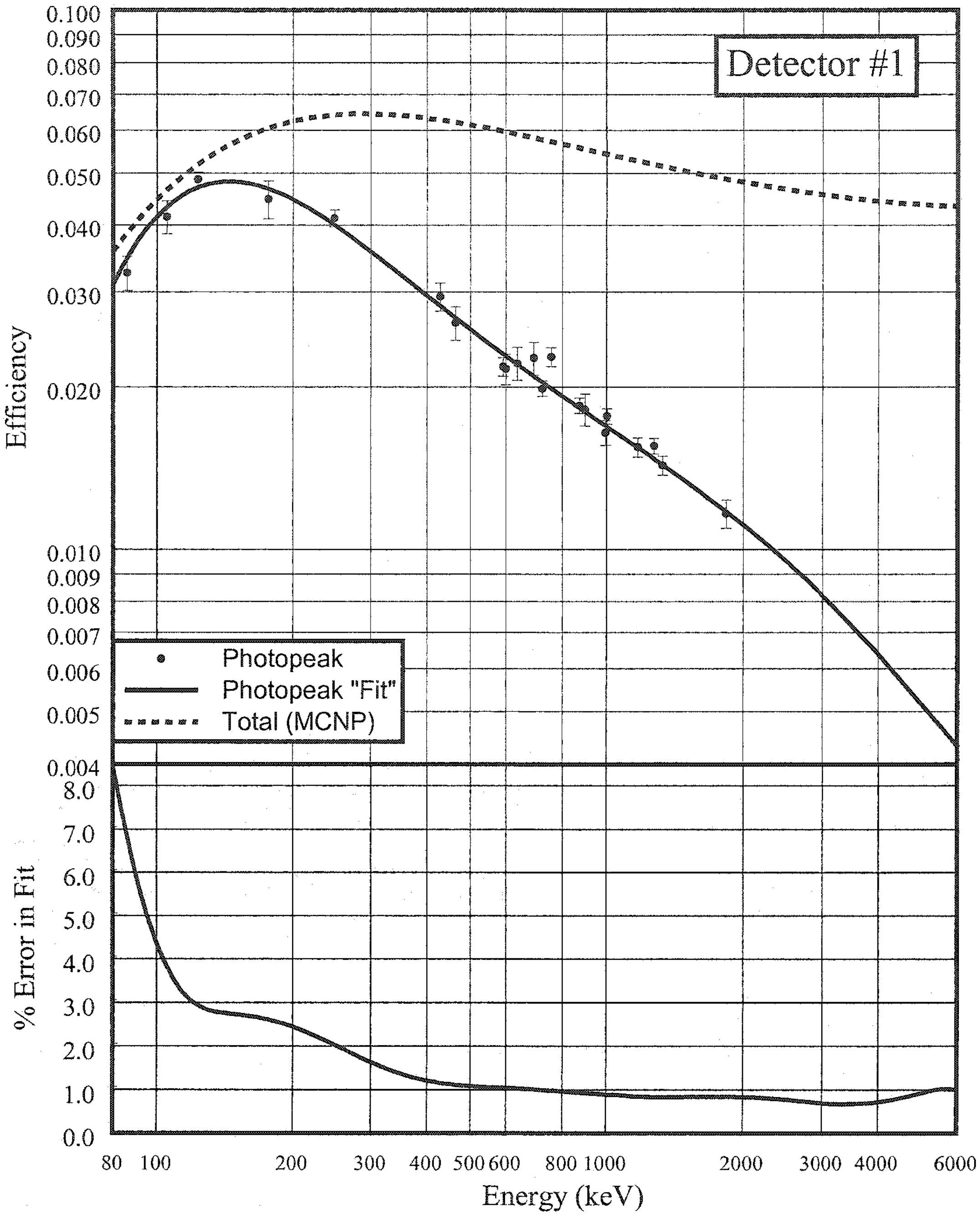

Fig. 3.8 Efficiency calibration spectra for the Ge-1 detector. The upper section shows the log-log plot of efficiency versus energy. The solid line shows the fit photopeak efficiency curve, and the dashed line shows the total efficiency curve. The lower section shows the uncertainty in the calibration as a function of energy in log- log scale.

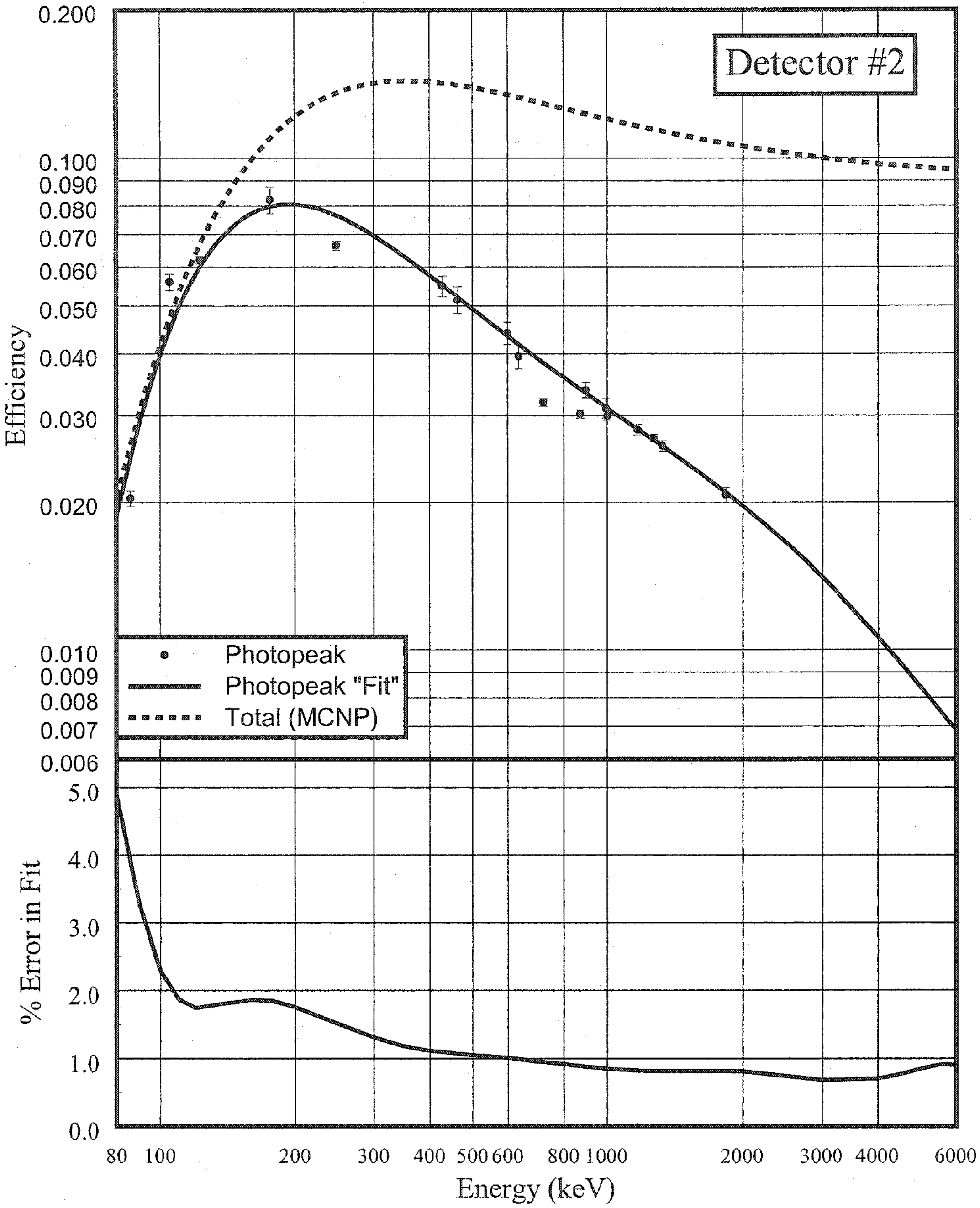

Fig. 3.9 Efficiency calibration spectra for the Ge-2 detector. The upper section shows the log-log plot of efficiency versus energy. The solid line shows the fit photopeak efficiency curve, and the dashed line shows the total efficiency curve. The lower section shows the uncertainty in the calibration as a function of energy in log- log scale

3.5 Experimental Results

Several timing cycles and A1200 settings were used to identify and positively associate γ rays with their radioactive source. With the A1200 set for maximum ^{41}P production, but with the ^{44}Cl centered at the focal plane, data were collected using three timing cycles. With a 2500 ms growth and 2500 ms decay timing cycle (long cycle), data were collected for 9.5 hours. This allowed a precise determination of the half-life of (672 ± 18 ms) for ^{44}Cl. A 1000 ms growth and 1000 ms decay timing cycle (short cycle) was used to enhance the events for ^{44}Cl decay relative to those from longer-lived nuclides. For a time duration of 4.1 hours, data were collected with this timing cycle. This provided about the same counts in the spectra for the primary γ-ray lines from ^{44}Cl from both timing cycles, thus allowing assignment of the observed γ rays to particular decays. Saturation data were collected at the end of the experiment. During this measurement, the beam was first implanted for a period of 25 minutes into a single catcher before data were collected, with beam still being implanted, for a period of 21 minutes

CHAPTER IV

DATA ANALYSIS

In section 4.1, the procedure of calculating the “f” value and hence the branching ratio for the ^{44}Cl decay is presented. The branching ratio was needed to calculate the intensities and the log(ft) values for γ-ray transitions, which in turn were used to establish the level scheme for ^{44}Cl decay presented in the next chapter. In section 4.2 the γ ray coincidence relationships and gated spectra are presented. In section 4.3 the half-life of the ^{44}Cl is presented.

4.1 Branching Ratio

The ratio of the probability of decay by a certain mode to the probability of decay by any mode is known as the branching ratio [1,2,18]. In this experiment, the fact that the ^{44}Cl was the only member of the A=44 mass chain separated, made it possible to estimate the ground state feeding for its decay from a saturation spectrum. Since all γ rays within the β branch, each mass chain that is, have the same ratio of relative intensity to branching ratio, called the “f” value, we only need this value to relate a known branching ratio within a decay chain to the intensity of a particular γ transition, the 1157-keV transition in this study, in the unknown decay.

Relative intensities of the 1703- and 1886-keV γ rays from ^{44}Ar decay (Fig. 4.1), and the 1024, 1126-, and 1157-, 1499-, 2150-, and 2518-keV γ rays of ^{44}K decay (Fig. 4.2), were used to find the "f" value for the A= 44 decay chain. The procedure used is as follows:

A) First, the intensity (I_γ) of each γ ray from ^{44}Ar and ^{44}K decay relative to the intensity of the 1157-keV γ ray from ^{44}Cl decay was determined according to

$$I_\gamma = 100\left(\frac{A_\gamma / \varepsilon_\gamma}{A_{1157} / \varepsilon_{1157}}\right) \qquad (4.1)$$

where A_γ and A_{1157} are the number of counts of the particular γ ray and the 1157 keV γ ray from ^{44}Cl decay, and ε_γ is the relative efficiency.

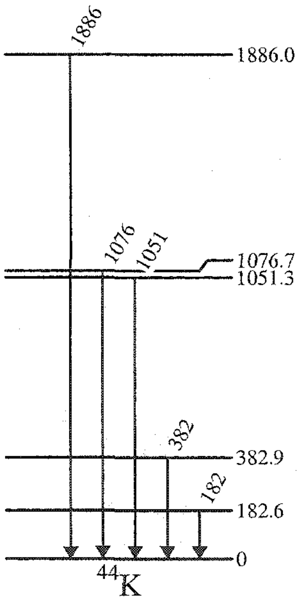

Fig. 4.1 Partial level scheme of ^{44}Ar decay into ^{44}K showing the 1703- and 1886-keV γ rays used in determining the "f" value for the ^{44}Cl.

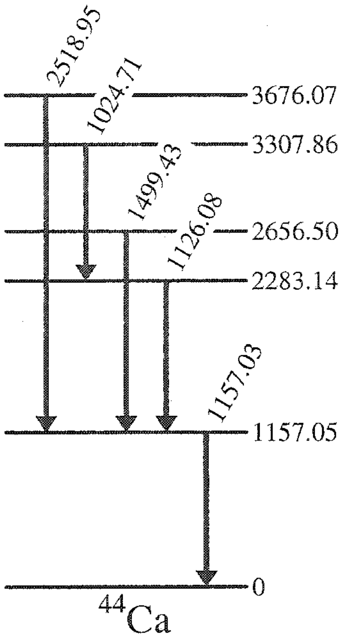
2518.95
1024.71
1499.43
1126.08
1157.03
3676.07
3307.86
2656.50
2283.14
1157.05
0
^{44}Ca

Fig. 4.2 Partial level scheme of ^{44}K decay into ^{44}Ca. The 1157-, 1126-, 1499-, 1024-, and 2518-keV γ rays were used in determining the "f" value for the ^{44}Cl decay.

B) Second, the relative intensity of each γ ray was divided by its known branching ratio (BR) to obtain the "f" value

$$f = \frac{I_\gamma}{BR} \qquad (4.2)$$

where the branching ratio (BR) of any γ ray within the branch is given by

$$BR = I_{R\gamma} C \qquad (4.3)$$

where $I_{R\gamma}$ is the relative intensity for the particular decay (i.e., what you would find listed in the Table of Isotopes), and the constant C is a normalization factor peculiar to the decay. For ^{44}Ar, C has a value of 0.66 ±0.09, while it is 0.58 ±0.09 for ^{44}K [24].

C) Third, the "f" value from Eq. 4.2 was divided by the saturation fraction, 0.87 for ^{44}Ar, and 0.45 for ^{44}K [24]. This calculation was done for both detectors, and the average was found. Results of the "f" value calculation for the Ge-2 detector are shown in Table 4.1. It was discovered that the "f" value for ^{44}Ar was invalid since it would result in a branching ratio of greater than 100%. Consequently, it was determined that the published branching ratio for ^{44}Ar is in error and that only the value from the ^{44}Cl decay would be used. Therefore, based on a relative intensity of 100 for the 1157-keV γ ray the branching ratio is found from

$$B.R_{1157} = \frac{1}{f} \qquad (4.4)$$

The value of the branching ratio, 0.90 ± 0.14, determined by this technique will be compared with the value determined by an alternate method in the next chapter. Based on the branching ratio, the absolute intensity for each γ ray from the ^{44}Cl decay can be determined. These intensities will be used to calculate the log(ft) values of the energy levels from the ^{44}Cl decay as will be discussed later. This information in turn allows estimation of the spin/parity of each level in the decay.

Table 4.1 The “f” values calculated from γ rays from ^{44}Ar and ^{44}K decay relative to the intensity of 1157 keV from ^{44}Cl decay. The energy 1157 keV is the reference γ ray from ^{44}Cl. The terms in the caption are defined in the text.

^{44}Ar	Area [b]		$I_{R\gamma}$ [c]		ε_γ [d]		I_γ [e]		B. R.[f]		f [g]	
E_γ	Value	Error	Value	Error	Value	Error	Value	Error	Value	Error	Value	Error
1157.74 [a]	685	30			1.00	0.01	100.0					
1703.40	190	14	85.6	0.1	0.78	0.01	35.7	3.1	56.5	7.7	0.6	0.1
1886.00	114	11	47.7	0.1	0.75	0.01	23.0	2.5	31.5	4.3	0.7	0.1

^{44}K	Area [b]		$I_{R\gamma}$ [c]		ε_γ [d]		I_γ [e]		B. R.[f]		f [g]	
E_γ	Value	Error	Value	Error	Value	Error	Value	Error	Value	Error	Value	Error
1157.74	685	30			1.00	0.01	100.0					
1024.71	21	6	11.5	0.2	1.08	0.01	2.8	0.8	6.7	1.0	0.4	0.1
1126.10	28	7	13.1	0.2	1.02	0.01	4.0	1.0	7.6	1.2	0.5	0.1
1157.03	206	114	100.0	0.1	1.00	0.01	30.1	16.7	58.0	9.0	0.5	0.3
1499.49	26	7	13.5	0.5	0.85	0.01	4.5	1.2	7.8	1.3	0.6	0.2
2150.76	79	10	39.1	0.8	0.66	0.01	17.6	2.4	22.7	3.6	0.8	0.1
2518.95	24	6	16.7	0.3	0.58	0.01	6.1	1.5	9.7	1.5	0.6	0.2

a. Most intense γ ray from ^{44}Cl decay.
b. Measured area of γ ray peak in saturation spectrum.
c. Known relative intensity within the particular decay.
d. Efficiency relative to that of the 1157-keV ray from ^{44}Cl decay.
e. Intensity relative to that of the 1157-keV ray from ^{44}Cl decay.
f. Known branching ratio for the γ ray. See text.
g. Ratio of relative intensity to branching ratio.

4.2 γ Ray Spectra and Coincidence Relationships

For each setting of the system (A1200 and timing cycle), β-gated γ-ray energy spectra were extracted from the event data. These spectra, for each detector, were fit to provide a complete set of all observed γ rays. Detailed comparisons between these sets (long cycle and short cycle) permitted us to associate observed γ rays with a particular decay. Additional information on γ-γ coincidence relationships was also extracted from the full event data set. Based on this information, 11 γ rays were associated with the decay of ^{44}Cl. A γ ray at 1157 keV was the strongest γ ray observed associated with the decay of the ^{44}Cl, and it corresponds to the first excited state of ^{44}Ar. Table 5.1 in the next chapter shows the average results of the two germanium detectors on the measured γ-ray energies and intensities, placements, and coincidence relationships. The intensities shown include corrections due to coincidence summing that are based on the proposed level scheme. Fig.4.3 shows a β-gated γ-ray singles spectrum for the Ge-1 detector.

By using standard techniques, the background–subtracted coincidence γ-ray spectra were obtained. These coincidence spectra were gain shifted to 1 channel per keV and summed for both detectors. Fig 4.4 shows the coincidence spectra gated on 852, 1157, 2010, and 2796 keV γ rays respectively. The energies of the coincident γ rays are indicated in the spectra. These four γ rays are the strongest observed in the decay and form the basis for the level scheme. Fig. 4.5 shows the coincidence spectrum for the other γ rays observed in the decay.

The strongest γ rays from the ^{44}K and ^{44}Cl decays, 1157.03 and 1157.74 keV, respectively were difficult to differentiate because they were only 0.7 keV apart and appeared as an unresolved doublet. To differentiate between the two γ rays, the following was used in the process of fitting the two peaks. The centroid of the γ ray from ^{44}K decay was kept fixed to the known energy (based on the calibration), and its height was varied until the ratio of the intensities (areas) of the two spectra was equal to the ratio of the normalization factor from ^{44}K decay to that of ^{44}Cl decay, then the position of the centroid of the 1157 keV from the ^{44}Cl decay was recorded.

This procedure was done for both germanium detectors, and the values were used to calculate the "f" value and the branching ratios and intensities of the γ rays from ^{44}Cl decay as discussed in the next chapter.

Based on the γ-ray singles and coincidence data, 11 γ rays were placed in the decay scheme for ^{44}Cl that populated six excited states in ^{44}Ar. The level scheme for the ^{44}Cl decay is shown in Fig. 5.1 of the next chapter.

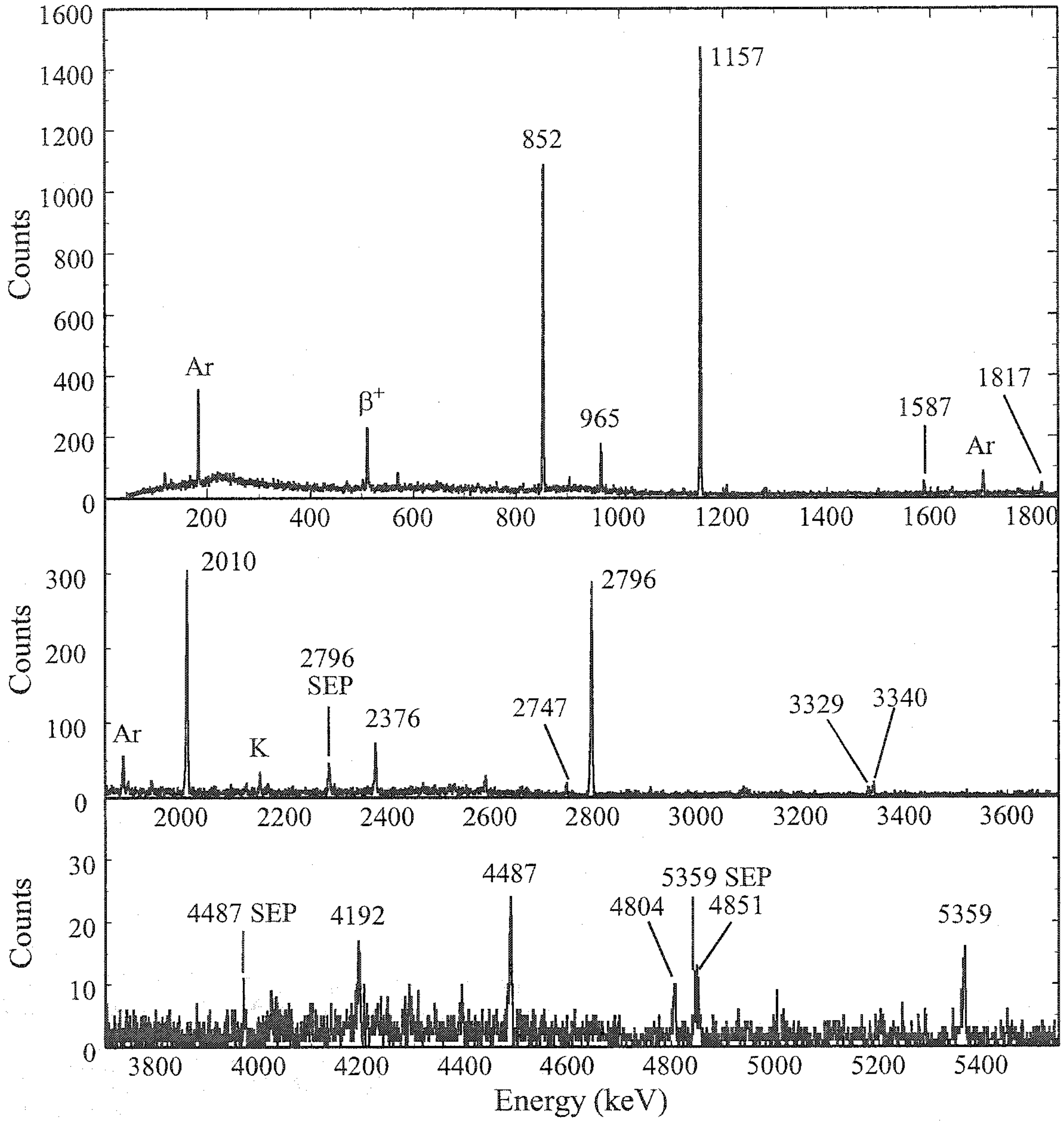

Fig. 4.3 β-gated γ-ray singles spectrum for the Ge-1 detector. Lines assigned to the decay of ^{44}Cl decay are labeled with their energy in keV. Single Escape Peaks (SEP) are labeled with the energy of the original γ ray followed by SEP.

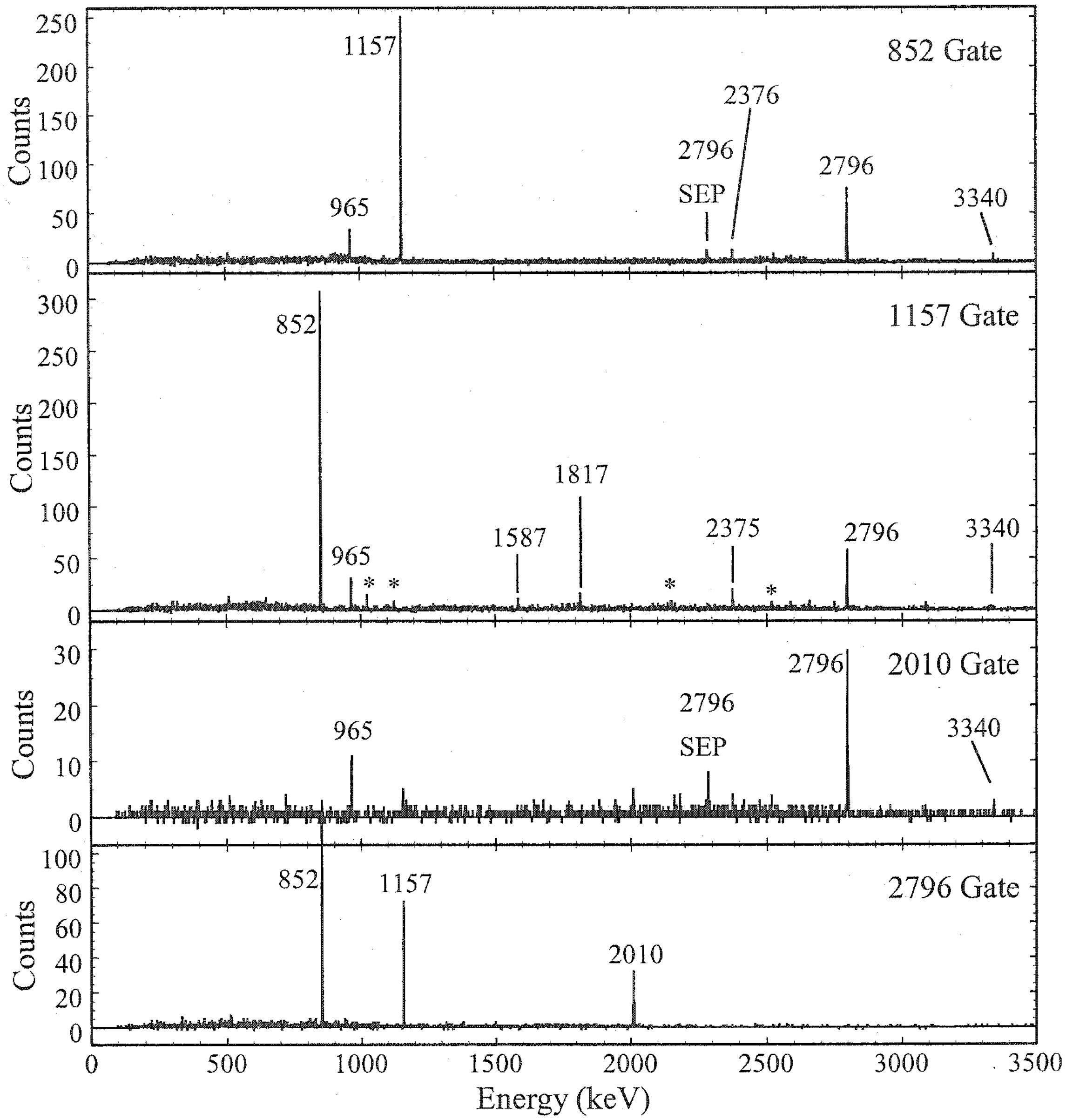

Fig. 4.4 Background-subtracted γ ray coincidence spectra gated on the 852, 1157, 2010, and 2796 keV γ rays.

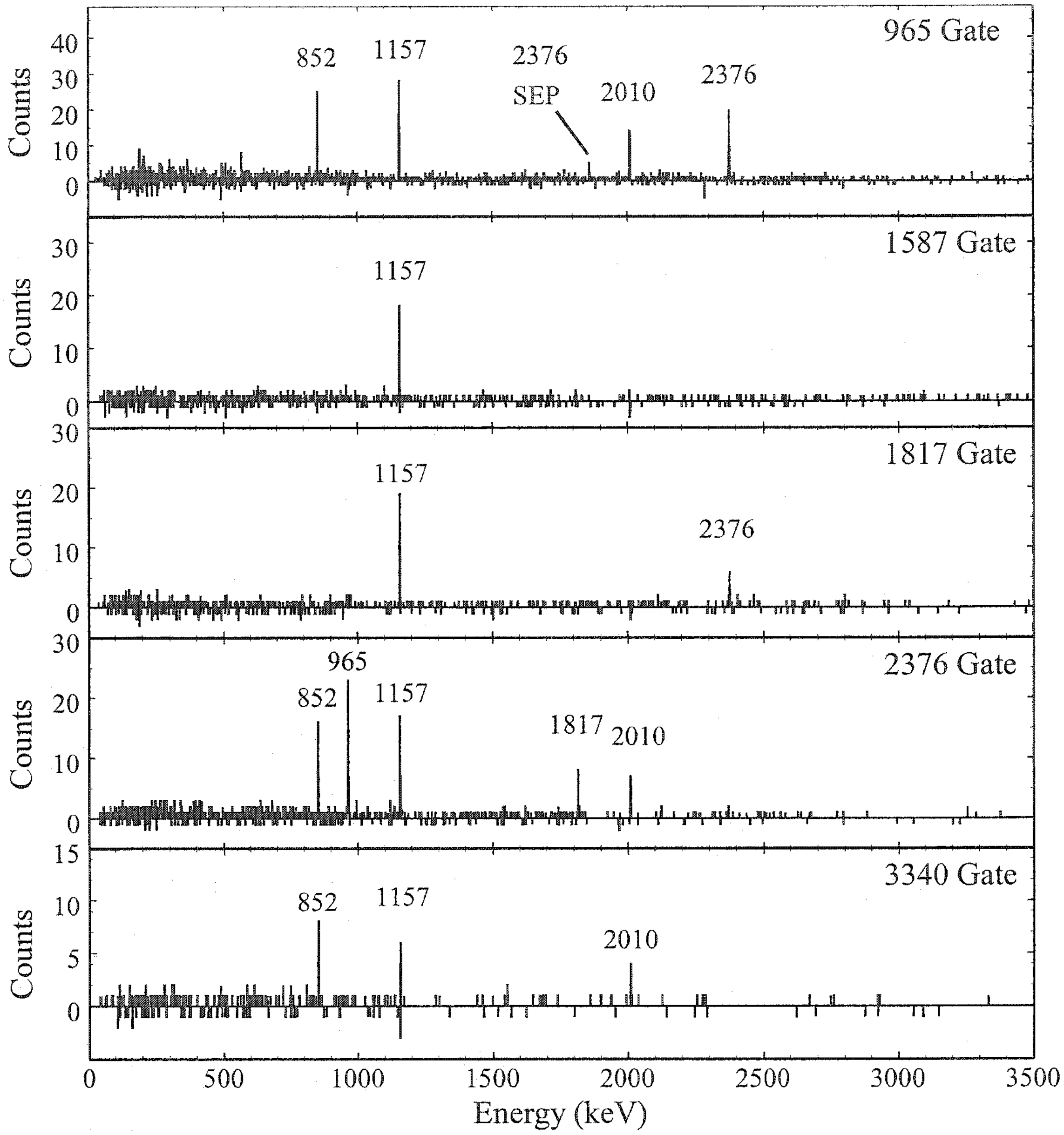

Fig. 4.5 Background–subtracted γ ray coincidence spectra gated on the 965, 1587, 1817, 2376 and 3340 keV γ rays.

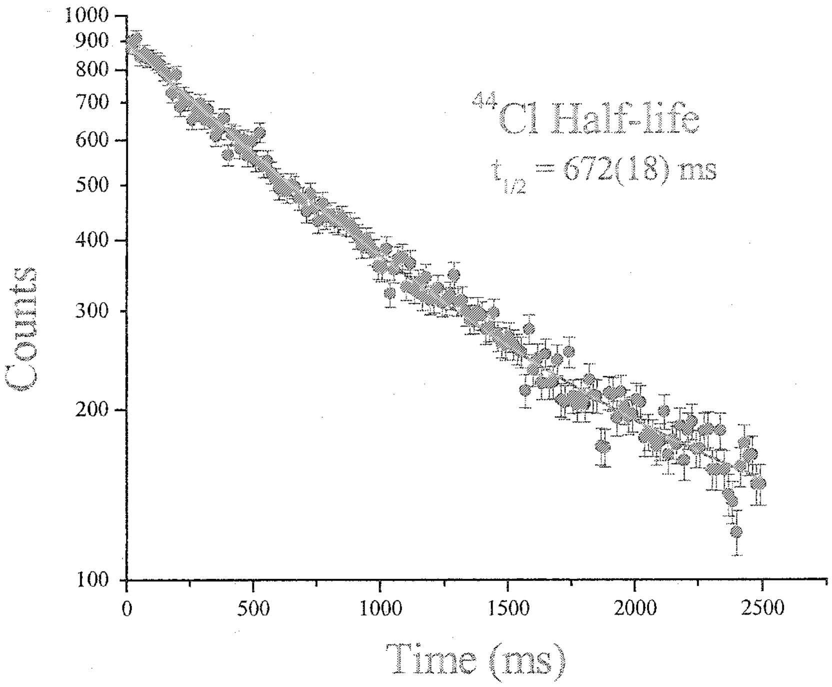

Fig. 4.6 Half-life curve for the decay of the 852 and 2010, and 2796 keV γ rays associated with ^{44}Cl β decay.

4.3 Half-life of ^{44}Cl

The half-life of ^{44}Cl was determined using a time spectrum gated by the 852-, 2010, and 2796 keV γ rays. Using two decaying exponential functions, where parameters for the background were held fixed, we did the fit for this time spectrum. The spectrum obtained in this procedure is shown in Fig. 4.6. From the time spectrum decay, the half-life value of 672 ± 18 ms was obtained. In comparison, the measurement by Sorlin *et al.* of the β-decay of ^{44}Cl nuclei found the half-life to be 434 ± 60 ms [13]. Gating on 852 and 2010 and 2796 keV γ rays assures the correct identification of the ^{44}Cl nucleus, which leads to a more precise measurement of the half-life.

CHAPTER V

LEVEL SCHEME DEVELOPMENT

5.1 Introduction

Table 5.1 contains the energies, relative intensities, placements, and the coincidence relationships for the γ rays associated with the decay of ^{44}Cl. The level scheme for the β decay of ^{44}Cl into ^{44}Ar was developed, as shown in Fig. 5.1, based on the γ γ coincidences and the energy sums. Details on how the level scheme was developed will be given in the following sections. This will include details on finding the absolute feeding (B.R.) and the interpretations of the level scheme.

Table 5.2 contains information on each energy level and its corresponding spin/parity, net feeding, and log(ft) value as determined from the level scheme. The feeding intensities' column is divided into three columns: in, out, and net. The "in" column contains the sums of the summing corrected relative intensities of γ rays feeding into that level. The "out" column contains the sums of the summing corrected relative intensities of γ rays decaying out of that level. The "net" column contains the normalized difference between the "in" and "out" intensities, i.e the outcome of the subtraction of the "in" intensity from the "out" intensity was multiplied by the normalization factor. The normalization factor, which was found to be 0.67 ± 0.06, was obtained by dividing 100

Table 5.1 Energies of the γ rays placed in the ^{44}Ar level scheme, their relative intensities, their placements, and their coincidence relationships.

Energy (KeV)	Relative Intensity (%)	Placement	Coincidence
852.58±0.05	65.4 ± 1.4	2010→1157	965, 1157, 2376,2796, 3340
965.09±0.05	10.8 ± 0.4	2975→2010	852,1157,2010, 2376
1157.72±0.07	100.0± 2.0	1157→0	852, 965,1817, 1587, 2376
1587.93±0.11	4.4 ± 0.4	2745→1157	1157
1817.60±0.12	4.7 ± 0.6	2975→1157	1157, 2376
2010.29±0.14	45.5 ± 1.0	2010→0	965, 2796, 3340
2375.61±0.12	11.7±1.0	5351→2975	852, 965, 1157, 1817, 2010
2747.04±0.18	1.6± 0.3	2747→0	
2796.29±0.06	61.0 ± 4.5	4807→2010	2010, 852, 1157
3340.33±0.17	2.5 ± 0.5	5351→2010	852, 1157, 2010
5359.00±0.05	3.5±0.7	5351→0	

by the sums of the difference between the "in" and "out" intensities. This assumes no significant feeding to the ground state. The log(ft) values for the energy levels were obtained by using the nuclear structure calculational tools from the National Nuclear Data Center (NNDC) website [26].

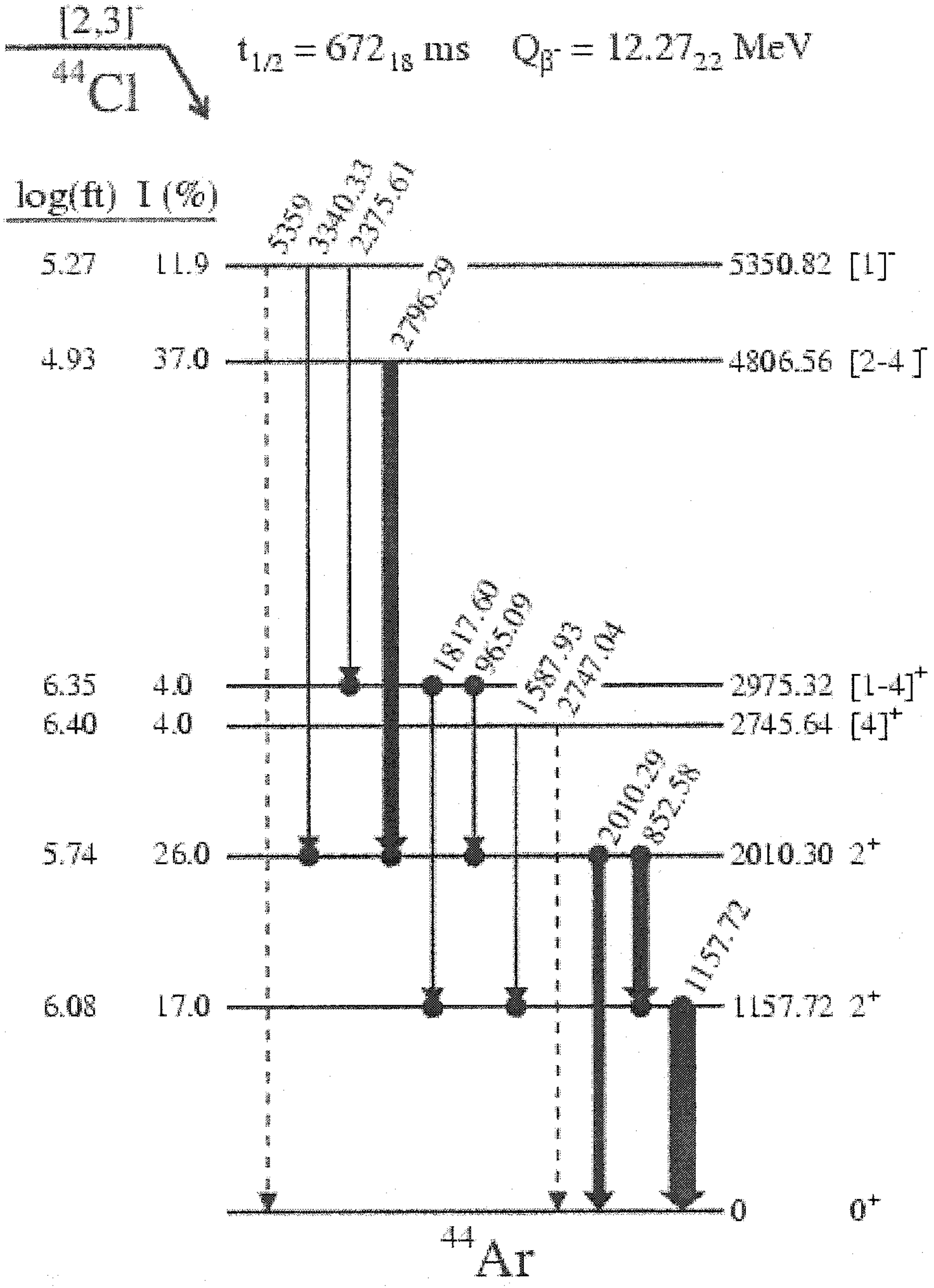
[2,3]⁻
44Cl
t1/2 = 672 18 ms
Qβ- = 12.27 22 MeV
log(ft)
I (%)
5.27
11.9
4.93
37.0
6.35
4.0
6.40
4.0
5.74
26.0
6.08
17.0
5359
3340.33
2375.61
2796.29
1817.60
965.09
1587.93
2747.04
2010.29
852.58
1157.72
5350.82 [1]⁻
4806.56 [2-4]⁻
2975.32 [1-4]⁺
2745.64 [4]⁺
2010.30 2⁺
1157.72 2⁺
0
0⁺
44Ar

Fig. 5.1 Level scheme for ^{44}Ar as determined from ^{44}Cl β decay. The width of the transition is proportional to the relative intensity of the γ ray.

Table 5.2 Energy levels and corresponding spin/parity, feeding, and log(ft) values.

Levels [a]	J^{π} [b]	Feeding			log(ft)
		In	Out	Net	
1157.72±0.07	2^+	74.6±1.5	100.0±2.0	17.0±1.7	6.08±0.05
2010.30±0.07	2^+	72.1±4.5	105.6±2.1	26.0± 3.0	5.74±0.06
2745.64±0.12	4^+		5.8± 0.5	4.0 ± 0.3	6.40±0.04
2975.32±0.08	$(1,2,3,4)^+$	9.6 ± 0.8	13.9 ± 0.6	4.0±.0.7	6.35±0.08
4806.56±0.09	$(2,3)^-$		55.0± 4.0	37.0± 2.7	4.93±0.03
5350.82±0.12	$(1,2,3,4)^-$		15.8±1.0	11.9±0.8	5.27±0.03

a. Levels' energies from least squares fit at γ-ray energies
b. Estimated J^{π} values from measured log(ft) values

5.2 Ground State of $^{44}_{17}\mathrm{Cl}_{27}$

The spherical shell model indicates that the ground state of the odd-odd ^{44}Cl must come from coupling of single nucleons in the $\pi d_{3/2}$ and $\nu f_{7/2}$ subshells resulting in the possible state of $(2,3,4,5)^-$, with the proton occupying a positive parity state and the neutron occupying a negative parity state. If we have slight prolate deformation as observed for other nuclides in this region, then we will have a $\pi\, {}^1\!/_2[210]\otimes\nu\, {}^7\!/_2[421]$ configuration, which yields $(3,4)^-$ states. If deformation is large enough it is possible for the $\nu\, {}^1\!/_2[300]$ state to drop lower, which yields $\pi\, {}^1\!/_2[200]\otimes\nu\, {}^1\!/_2[300]$ or $(0,1)^-$ states. Since 100% of the β intensities feed the excited states as shown in Fig.5.1, or in other words there is no feeding to the ^{44}Ar ground state, then the third possibility is rejected. The lack of feeding to the 0^+ ground state of the even-even ^{44}Ar strongly suggests a 3^- state, but a 2^- state cannot be rejected. The log(ft) value of 6.08 measured for the 1157-keV level indicates that this a first forbidden transition, well established by other experiments. This will limit the ^{44}Cl ground state to the 2^- or 3^- state. However, the experimental deformation values favor the 3^- assignment.

5.3 Level Structure of ^{44}Ar

I) Level at 1157 keV

The 1157 keV γ ray is the strongest γ ray observed in the decay and is placed as depopulating the first excited state. This is supported by the observation of 2_1^+ state at an energy of 1144±17 keV by H. Scheit *et al.* [6] in intermediate-energy Coulomb excitation experiments. This is also consistent with the 2_1^+ first excitation energy at 1110±80 keV and 1158 keV observed by S. Wan [15] and B. Fornal *et al.* [16], respectively. In another experiment, using proton scattering, H. Scheit *et al.* [17] assigned an energy of 1167±40 keV to the 2_1^+ state. These observations indicate that the observed γ ray at 1157 keV from ^{44}Cl β decay depopulates the 2_1^+ state in ^{44}Ar.

II) Level at 2010 keV

As shown in Fig 5.1, the level 2010 at keV is established by the observation of a strong coincidence between the 852-keV and the 1157-keV γ rays. The observation of the crossover transition at 2010 keV plus its lack of coincidence (see Fig. 4.4 coincidence gate spectrum for 2010) with either the 852 or 1157-keV γ rays confirms this placement. J. Retamosa *et al.* [14] in theoretical calculations within the frame work of the shell model predicted the 2_2^+ state to be at an energy level of 1900 keV. Experimentally, the log(ft) value of 5.74 is consistent with a first forbidden transition. With $\Delta J = 0,1$ and $\Delta\pi = -$ for these transitions, this implies that it is possible to assign it as a 1^+ state if the ^{44}Cl ground state is 2^-. However, since the favored ^{44}Cl ground state is 3^-, it is more likely this is a 2^+ state. Hence the theoretical and experimental evidence suggest that this is the 2_2^+ state [14,16].

III) Level at 2745 keV

The level at 2745 keV is established by the observation of a coincidence between the 1587 keV and the 1157 keV γ rays, as shown in Fig. 4.4. B. Fornal *el al.* [16] suggested a 4^+ state at an energy 2746 keV, whereas S. Wan *et al.* [18] observed a 4^+ state at 2610±16 keV. J. Retamosa *et al* [14] in theoretical calculations predicted a 4^+ state at 2480 keV. The log(ft) value of 6.40 for the 2745-keV level is in agreement with a first forbidden transition, giving the possibility of $(3,4)^+$ state. The energy ratio $2745/1157 = 2.37$ is consistent with the value of the ratio $E(4_1^+)/E(2_1^+)$ shown in the theoretical background of Chapter 2 for an anharmonic vibrator. Also, the equation $E4_1^+ \approx 2E2_1^+ + 0.4E2_1^+$ is consistent with the value for this level [20]. This suggests a predominantly vibrational structure, with the 2745-keV level as the 4^+ member of the two phonon triplet.

IV) Level at 2975 keV

The level at 2975 keV is established by the observation of a coincidence between the 965 keV and the 852, 1157, and 2010 keV γ rays, as shown in Fig. 4.5. The theoretical calculations by J. Retamosa *el al.* [14,16] suggested a 3^+ state at an energy immediately higher than the 2746-keV level. With a log(ft) value of 6.35, the energy level at 2975 keV is consistent with a first forbidden transition, which gives the possibility of a $(1,2,3,4)^+$ state.

V) Level at 4807 keV

The level at 4807 keV is established by the observation of a strong coincidence between the 2796 keV and the 852, 1157, and 2010 keV γ rays, as shown in Fig. 4.4. There is no previous information about this state. The low log(ft) value of 4.93 is consistent with an allowed transition $(\Delta J = 0,\pm 1; \Delta\pi = +)$, which gives the possibility for a $(1,2,3,4)^-$ state. However, since lower order transitions are more likely than higher order transitions, it is more probable that higher spin states are expected to be populated, a 3^- or 4^- state is more likely. The strong transition to the 2_2^+ state suggests a 2^- or a 3^- state.

VI) Level at 5351 keV

The level at 5351 keV is established by the observation of a coincidence between the 2376 keV, 965 keV and the 2010 keV γ rays, and also between 3340 keV, 852 keV, and the 1157 keV γ rays (See Figs. 4.4 and 4.5). There is no previous measurement of a state at an energy of 5351 keV. The log(ft) value of 5.27 is consistent with an allowed transition, which gives the possibility for the $(1,2,3,4)^-$ states. However the transitions to the 0_1^+ and 2_2^+ states indicate that both of these are E1 transitions, and hence suggest a 1^- state.

CHAPTER VI

DISCUSSION AND CONCLUSION

6.1 Comparisons with Shell Model of ^{44}Ar

Comparisons between the level scheme of ^{44}Ar predicted in theoretical studies and those based on experimental evidence have been made before [14,15,16]. In the following paragraphs is a comparison between the experimental level scheme from β decay obtained in this study and the previous theoretical calculations based on the shell model as presented in earlier papers [15,16]. Fig. 6.1 shows the comparison of the level schemes of ^{44}Ar, up to 3000 keV, obtained in this study and these theoretical calculations.

In this study, the first excited state, the 2_1^+ state, was observed at 1157 keV. H. Scheit *et al.* [6] assigned an energy of 1144±17 keV to the 2_1^+ state, and in another experiment using proton scattering, he assigned an energy of 1167±40 keV to the same state [17]. B. Fornal *et al.* [16] observed a similar level at 1158 keV for the 2_1^+ state, whereas S. Wan *et al.* [15] observed the same state at 1110±80keV.

The second excited state, the 2_2^+ state, in this study was observed at 2010 keV. S. Wan *et al.* [15] observed the same state at 1780±80 keV. The theoretical calculations, predict an energy of 1900 keV for this 2_2^+ state [14,15].

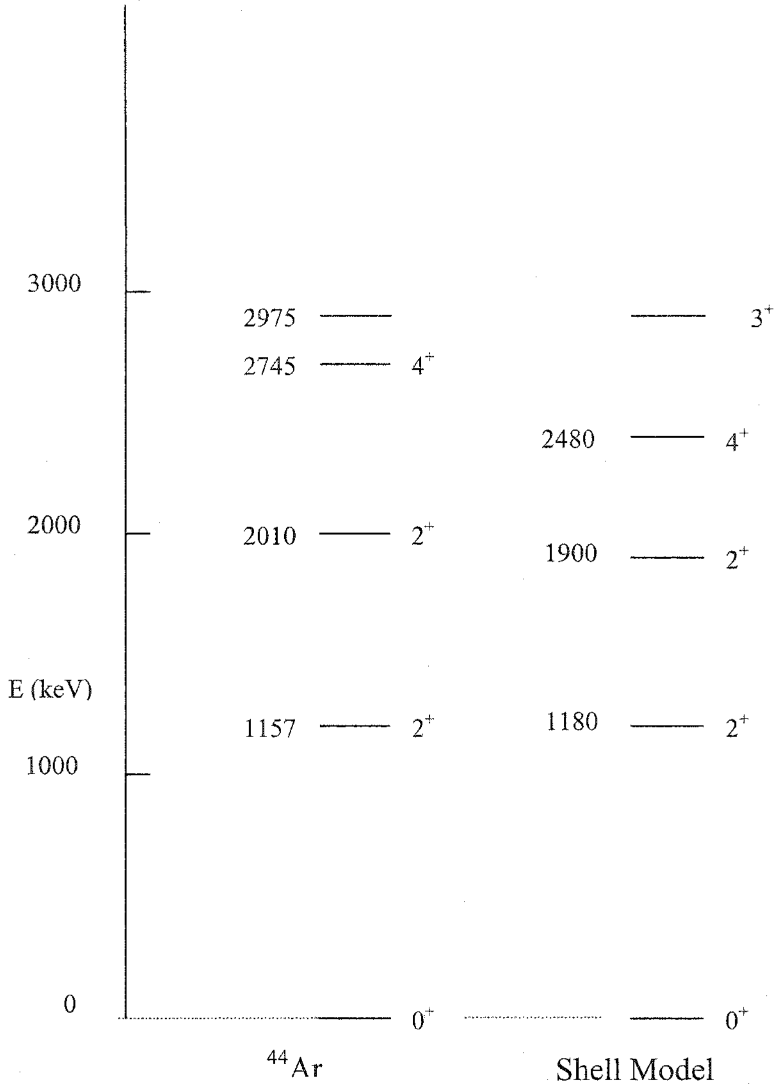
3000
2000
E (keV)
1000
0
2975
2745
4⁺
2010
2⁺
1157
2⁺
0⁺
3⁺
2480
4⁺
1900
2⁺
1180
2⁺
0⁺
44Ar
Shell Model

Fig. 6.1 Comparison of the level scheme of ^{44}Ar to the theoretical calculations [15,16]. Excitation energies are in keV.

The third excited state, the proposed 4_1^+ state, was observed at 2745 keV in this study. A state around the same energy was observed by S. Wan *et al.* [15] at 2610±160 keV, and at 2746 keV by B. Fornal *et al.* [16].

The fourth excited states observed at 2975 keV in this experiment, has not been observed experimentally before. However, the theoretical calculations [14,16] suggested a 3^+ state at an energy immediately higher than the state at 2746 keV.

The previous studies did not present results for any higher lying negative parity states corresponding to the levels at 4807 keV and 5351 keV found in this study.

6.2 Comparison between ^{42}Ar and ^{44}Ar

A comparison of the low energy structure between the even-even ^{44}Ar and the even-even ^{42}Ar is presented in Fig 6.2. The ^{44}Ar has 6 nucleons in the $\nu f_{7/2}$ subshell whereas the ^{42}Ar has 4 nucleons in the $\nu f_{7/2}$ subshell. The low-energy structure for both nuclei has been studied and measured through many reactions and techniques, which have resulted in energy level schemes with states up to 5351 keV for ^{44}Ar and 7600 keV for the ^{42}Ar. H. Scheit et al. [17] studied the ^{42,44}Ar unstable neutron-rich isotopes by proton scattering. They showed that the quadrupole deformation parameter $|\beta_2|$ for the 2_1^+ state of ^{42}Ar and ^{44}Ar were 0.32±0.05 and 0.31±0.05, respectively. Their results indicated that the deformation of the Ar isotopes changes from strongly oblate for ^{36}Ar to more prolate for ^{40,42,44}Ar. These similarities suggest the basic structure of the ^{42}Ar and ^{44}Ar isotopes should be alike.

In comparison, both ^{42}Ar and ^{44}Ar show possible anharmonic vibrational structure for energies up to 3.0 MeV. This manifested in fact that members of two-phonon states (2^+, 0^+, and 4^+) for ^{42}Ar were observed at lower energies corresponding to 2485-, 2511-,

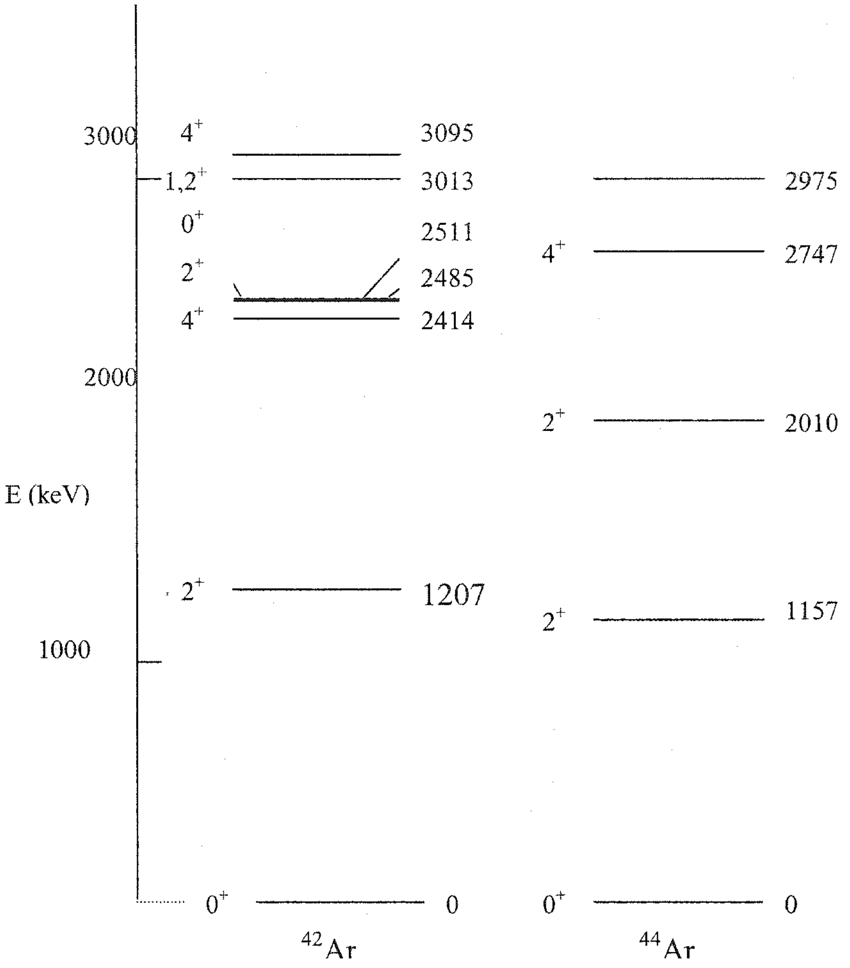
3000
2000
1000
E (keV)
4+ 3095
1,2+ 3013
0+ 2511
2+ 2485
4+ 2414
2+ 1207
0+ 0
42Ar
2975
4+ 2747
2+ 2010
2+ 1157
0+ 0
44Ar

Fig. 6.2 Comparison of the level scheme of ^{44}Ar to the level scheme of ^{42}Ar [7].

and 2414 keV respectively, in comparison to the typical values of 2535-, 2655, and 2897 keV respectively. For ^{44}Ar the possible 4^+ member of the two- phonon triplets was observed at an energy of 2745 keV in comparison to the typical value of 2777 keV. For ^{42}Ar, the observation of states near 3.0 MeV that are not members of one and two-phonon multiples indicate that other effects at higher energies dominate the structure. The low-energy structure of the ^{44}Ar also exhibits possible anharmonic vibrational characteristics up to 3.0 Mev. Since the 2_1^+ state of ^{44}Ar at 1157 keV is shifted down and the average energy of the two-phonon state is more than twice that of the 2_1^+ state, the energy separations between the expected two-phonon states are increased. The 2_2^+ state of ^{44}Ar at 2010 keV, with strong transitions to the 2_1^+ and the 0_1^+ states, is not a pure vibrational state, but also shows a shell model behavior.

6.3 Summary and Conclusion

This study "THE β^- DECAY OF ^{44}Cl" was based on an experiment conducted at the National Superconducting Laboratory (NSCL) at Michigan State University. In this study, the β decay of ^{44}Cl into the excited states of ^{44}Ar was studied. 11 γ rays were associated with the decay of ^{44}Cl and the half-life of ^{44}Cl was found to be 672 ± 18 ms. Based on the coincidence relationships and intensities, an energy level scheme of the observed γ rays was established with 6 levels up to 5351 keV.

A γ ray at 1157 keV was the strongest γ ray observed associated with the decay of the ^{44}Cl, and corresponds to the first excited state of the ^{44}Ar. A comparison between ^{42}Ar and ^{44}Ar up to excited state energies of 3000 keV was made. Despite the fact that the 2_1^+ state of ^{44}Ar at 1157 keV is lower than the 2_1^+ state of ^{42}Ar at 1207 keV, the structure of ^{44}Ar did not indicate pure vibrational states. Instead, with the exception of the state at 2010 keV which shows vibrational-shell model state, and the state at 2745 keV which is a 4^+ candidate of the two phonon triplets, the higher lying states of ^{44}Ar indicate a mixture of shell model states.

REFERENCES

[1] W. E. Burcham, F. R. S, " Nuclear Physics, an Introduction", McGraw-Hill Book Company, Inc., 1963, pp. 73, 361

[2] W. S. C. Williams, "Nuclear and Particle Physics", Oxford University Press, 1991, pp. 132

[3] X. Campi, H. Flocard, A. K. Kerman, S. Koonin, "Shape Transition in the Neutron Rich Sodium Isotopes", Nuc. Phys. A **251**, 1975, pp. 193-205

[4] T. Motobayashi, Y. Ikeda, Y. Ando, K. Leki, M. Inoue, N. Iwasa, T. Kikuchi, M. kurokawa, S. Moriya, S. Ogawa, H. Murkami, S. Shimoura, Y. Yanagisawa, T. Nakamura, Y. Watanabe, M. Ishihara, T. Teranishi, H. Okuno, R. F. Casten, "Large deformation of the very neutron-rich nucleus ^{32}Mg from intermediate-energy Coulomb excitation", Phys. Lett. B **364**, 1995, pp. 9-14.

[5] T. R. Warner, J. A. Sheikh, M. Misu, W. Nazarewicz, J. Rikovska, K. Heeger, A. S. Umar, M. R. Strayer, "Ground–State Properties of Exotic Si, S, Ar and Ca Isotopes", Nuc. Phys. A **597**, 1996, pp. 327-339

[6] H. Sheit, T. Glasmacher, B. A. Brown, P. D. Cottle, P. G. Hansen, R. Harkewicz, R. W. Ibbotson, J. K. Jewell, K. W. Kemper, D. J. Morrissey, M. Steiner, P. Thirolf, and M. Thoennessen, "New Region of Deformation: The Neutron-Rich Sulfur Isotopes", Phys. Rev. Lett. **77**, 1996, pp. 3967-3970.

[7] J. A. Winger, P. F. Mantica, R. M. Ronningen, and M. A. Caprio, "Low-Energy Structure of ^{40}S Through ^{40}P Decay", Phys. Rev. C **64**, 2001, pp. 064318-1-064318-11.

[8] R. E. Larson, and C. M. Gordon, "Production and Decay of ^{43}Ar and ^{44}Ar", Nucl. Phys. A**133**, 1969, pp. 237-240.

[9] J. Hudis E. Hagebø, and P. Patzelt, "^{43}Ar and ^{44}Ar", Nuc. Phys. A **151**, 1970, pp. 634-640.

[10] G. M. Crawley, W. F. Steel, J. N. Bishop, P. A. Smith, and Maripuu, "A Determination of the Mass and Some Energy Levels of the Nuclide ^{44}Ar", Phys. Lett. B **64**, 1976, pp. 143-146

[11] X. G. Zhou, X. L. Tu, J. M. Wouters, D. J. Vieira, Z. Y. Zhou, H. L. Seifert, V. G. Lind, "Direct Mass Measurements of the Neutron-Rich Isotopes of Chlorine Through Iron", Z. Phys. A **337**, 1990, pp. 361-.366

[12] X. G. Zhou, X. L. Tu, J. M. Wouters, D. J. Vieira, K. E. G. Lobner, H. L. Seifert, Z. Y. Zhou, and G. W Butler, "Direct Mass Measurements of the Neutron-Rich Isotopes of Fluorine Through Chlorine", Phys. Lett. B **260**, 1991, pp. 285-290.

[13] O. Sorlin, D. Guillemaud-Muller, R. Anne, L. Axelsson, D. Bazin, W. Bohmer, V. Borrel, Y. Jading, H. Keller, K. –L. Kratz, M. Lewitowicz, S. M. Lukyanov, T. Mehren, A. C. Muller, Yu. E. Penionzhkevich, F. Pougheon, M. G. Saint-Laurent, V. S. Salamatin, S. Shoedder, A. Wohr, "Beta-Decay Studies of Far From Stability Nuclei Near N = 28", Nucl. Phys. A **583**, 1995, pp. 763-768.

[14] J. Retamosa, E. Caurier F. Nowacki, and A. Poves, " Shell model study of the neutron –rich nuclei around N=28", Phys. Rev. C **55**, 1997, pp. 1266-1274

[15] S. Wan, J. Gerl J. Cub, J.M. Holeczek, P. Reiter, D. Schwalm, T. Aumann, K. Boretzky, W. DostalB. Eberlein, H. Emling, Ch. Ender, Th.W. Elze, H. Geissel, A. Grunschlob, R. Holezmann, N. Iwasa, Mkaspar, A Kleinbohl, O. Koschorrek, Y. Leifels, A. Leistenschcheider, I. Peter, H. Schaffner, C. Scheidenberger, R. Schubart, H. Simon, G. Stengel, A. Surowiec, H. J. Wollersheim, "In-beam - spectroscopy with relativistic radioactive ion beams" Eur. Phys. J. A **6**, 1999, pp. 167-174.

[16] B. Fornal, R. Broda, W. Krolas, T. Pawalt, J. Wrzesinski, D. Bazzaco, S. Lunardi, C. Rossi Alvaez, G. Viesti, G. de Angelis, M. Cinausero, D. Napoli, J. Gerl, E. Caurier, and F. Nowacki, "New states in ^{42,44}Ar isotopes from deep-inelastic heavy ion reaction studies", Eur. Phys. J. A **7**, 2000, pp. 147-140.

[17] H. Sheit F. Marechal, T. Glasmacher E. Bauge, Y. Blumenfeld, J. P. Delaroche, M. Girod, R. W. Kemper, J. Libert, B. Pritychenko, and T. Suomijarvi, "Proton scattering by the unstable neutron-rich isotopes ^{42,44}A", Phys. Rev. C **63**, 2000, pp. 014604-1-014604-8.

[18] Keneth S. Krane, "Introductory Nuclear Physics", John Wiley & Sons, 1988, pp. 116, 117,121, 123, 124

[19] http://hyperphysics.phy-astr.gsu.edu/hbase/nuclear/shell.html#c1

[20] Richard F. Casten, "Nuclear Structure from a Simple Perspective", Oxford University Press Inc., 2000 pp. 179-208, 332-346

[21] http://physun.physics.mcmaster.ca/~jcw/nucexp/sdbook/nilsson.pdf

[22] NSCL Operating Manual pp. 56-65.

[23] B. M. Sherrill, D. J. Morrissey, J. A. Nolen Jr., N. Orr, and J. A. Winger, "Initial Operating Experience with the A1200 Fragment Separator", Nucl. Instrum. Methods Phys. Res. B **56/57**, 1991, pp. 298-303.

[24] http://www.nndc.bnl.gov/

[25] Richard B. Firestone, "Table of Isotopes", John Wiley & Sons, Inc., 1996, pp. 155, 156.

APPENDIX A

ELECTRONICS AND LOGIC CIRCUITRY

Appendix A shows schematic diagrams of the electronics and logic circuitry of the experiment that was conducted at the National Superconducting Cyclotron Laboratory (NSCL) at Michigan State University in 1998. The title of the experiment was: "Nuclear Structure in the Heavy S, Cl, and Ar Region". The diagrams include beam monitoring electronics (Fig. A.1), beta detectors electronics (Fig. A.2 and A.3), germanium detectors and their logic circuitry (Fig. A.4).

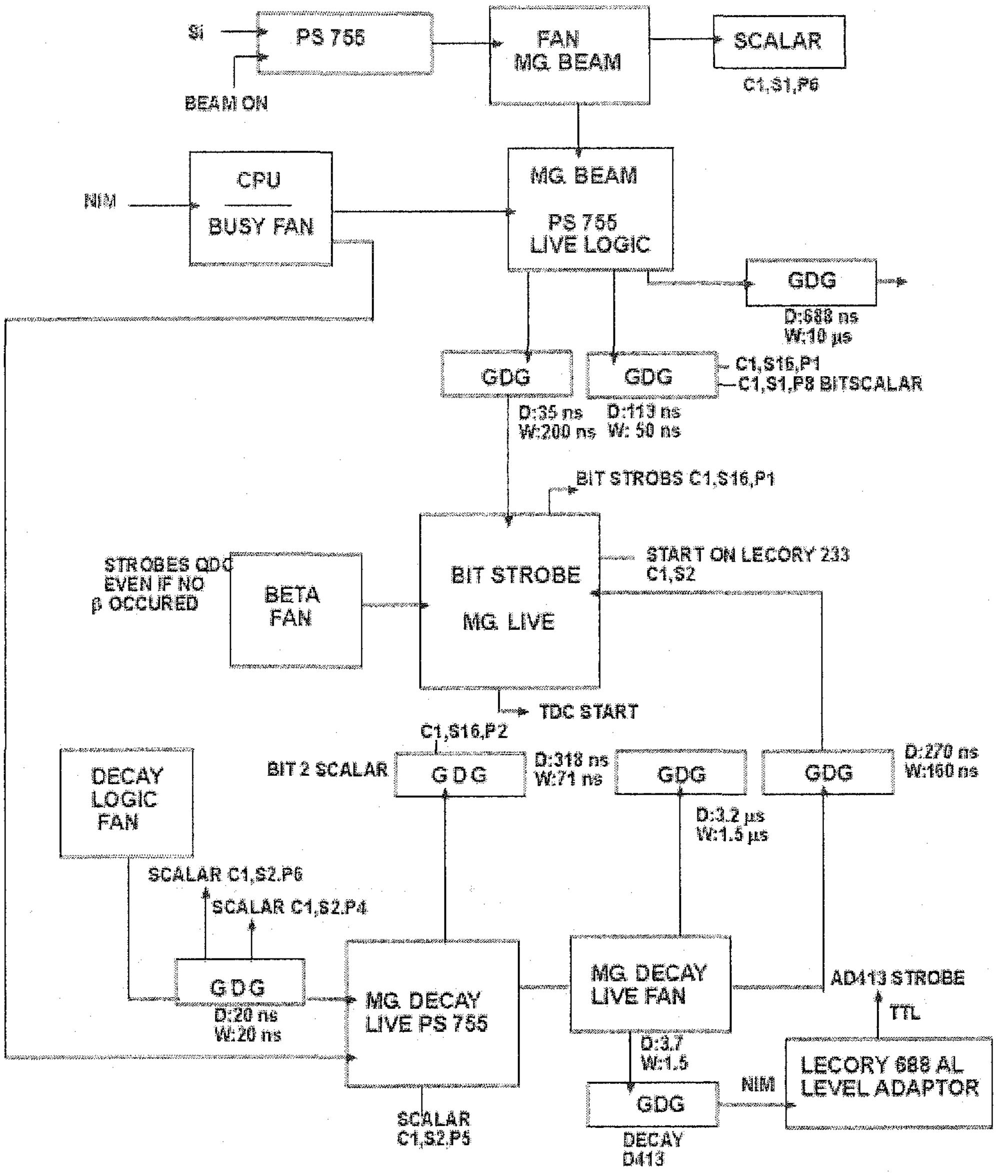
Si
PS 755
BEAM ON
FAN
MG. BEAM
SCALAR
C1,S1,P6
NIM
CPU
BUSY FAN
MG. BEAM
PS 755
LIVE LOGIC
GDG
D:688 ns
W:10 µs
GDG
GDG
C1,S16,P1
C1,S1,P8 BITSCALAR
D:35 ns
W:200 ns
D:113 ns
W: 50 ns
BIT STROBS C1,S16,P1
STROBES QDC
EVEN IF NO
β OCCURED
BETA
FAN
BIT STROBE
MG. LIVE
START ON LECORY 233
C1,S2
TDC START
C1,S16,P2
BIT 2 SCALAR
GDG
D:318 ns
W:71 ns
GDG
GDG
D:270 ns
W:160 ns
D:3.2 µs
W:1.5 µs
DECAY
LOGIC
FAN
SCALAR C1,S2.P6
SCALAR C1,S2.P4
GDG
D:20 ns
W:20 ns
MG. DECAY
LIVE PS 755
MG. DECAY
LIVE FAN
AD413 STROBE
TTL
D:3.7
W:1.5
GDG
NIM
LECORY 688 AL
LEVEL ADAPTOR
SCALAR
C1,S2,P5
DECAY
D413

Fig. A.1 Schematic diagram of the beam monitoring electronics and logic circuitry, and mastergate logic circuitry.

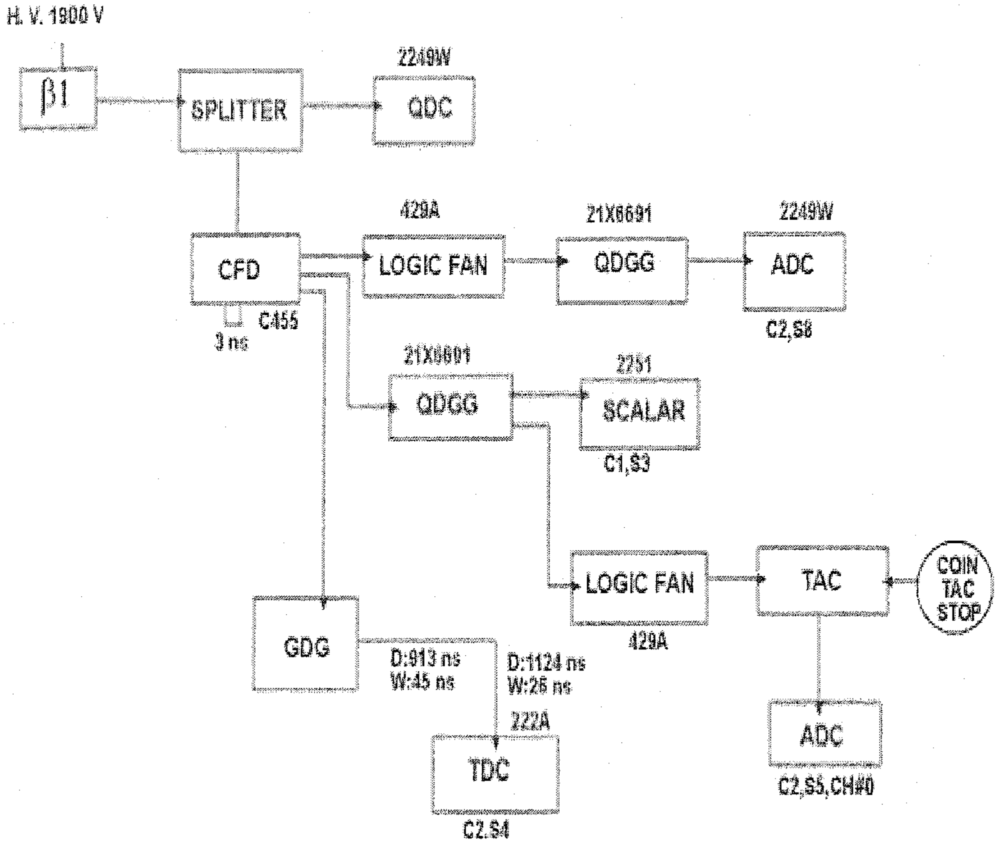
H. V. 1900 V
β1
SPLITTER
2249W
QDC
CFD
C455
3 ns
429A
LOGIC FAN
21X6691
QDGG
2249W
ADC
C2,S8
21X6601
QDGG
2251
SCALAR
C1,S3
LOGIC FAN
429A
TAC
COIN TAC STOP
GDG
D:913 ns
W:45 ns
D:1124 ns
W:26 ns
222A
TDC
C2.S4
ADC
C2,S5,CH#0

Fig. A.2 Schematic diagram of β2 detector electronics and logic circuitry.

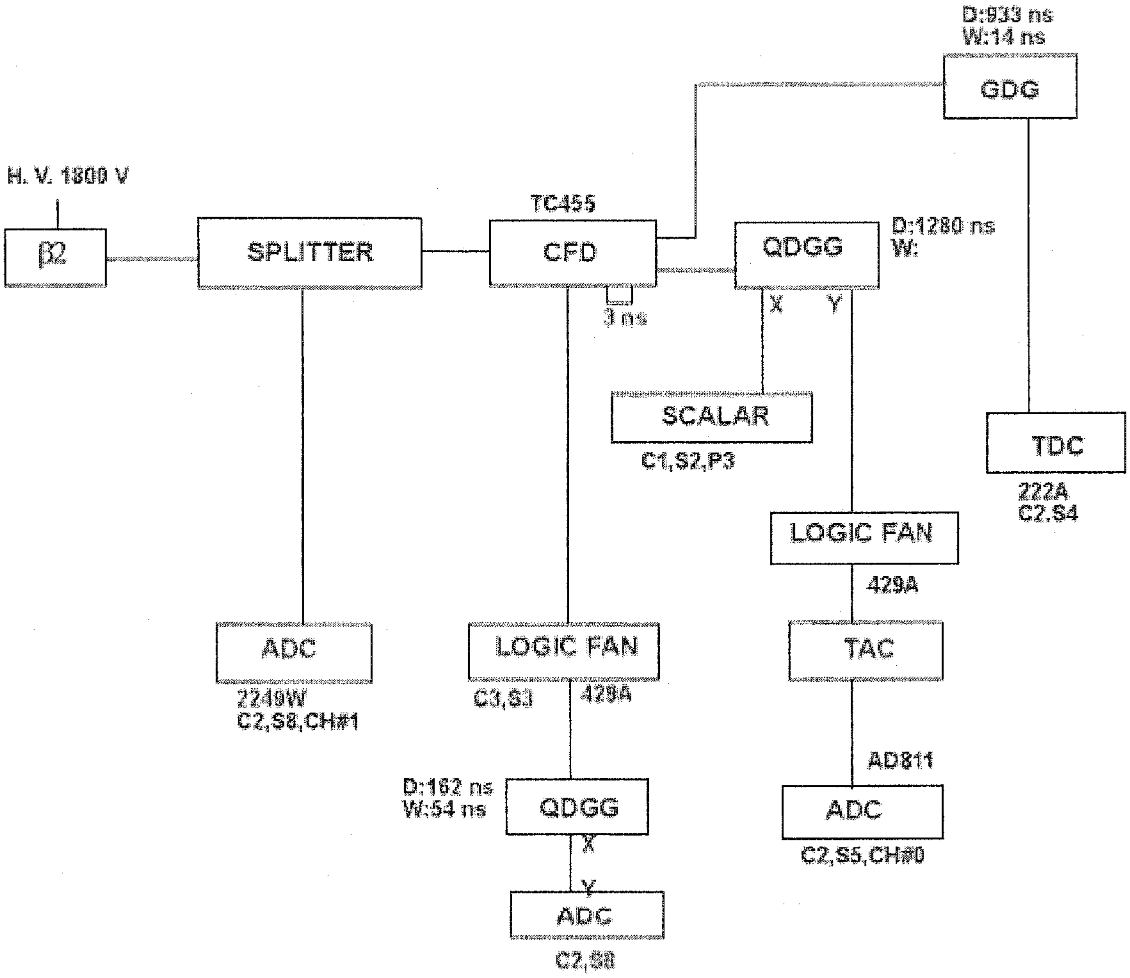
D:933 ns
W:14 ns
GDG
H. V. 1800 V
β2
SPLITTER
TC455
CFD
QDGG
D:1280 ns
W:
3 ns
X
Y
SCALAR
C1,S2,P3
TDC
222A
C2,S4
LOGIC FAN
429A
ADC
2249W
C2,S8,CH#1
LOGIC FAN
C3,S3
429A
TAC
AD811
D:162 ns
W:54 ns
QDGG
X
Y
ADC
C2,S5,CH#0
ADC
C2,S8

Fig. A.3 Schematic diagram of β2 detector electronics and logic circuitry.

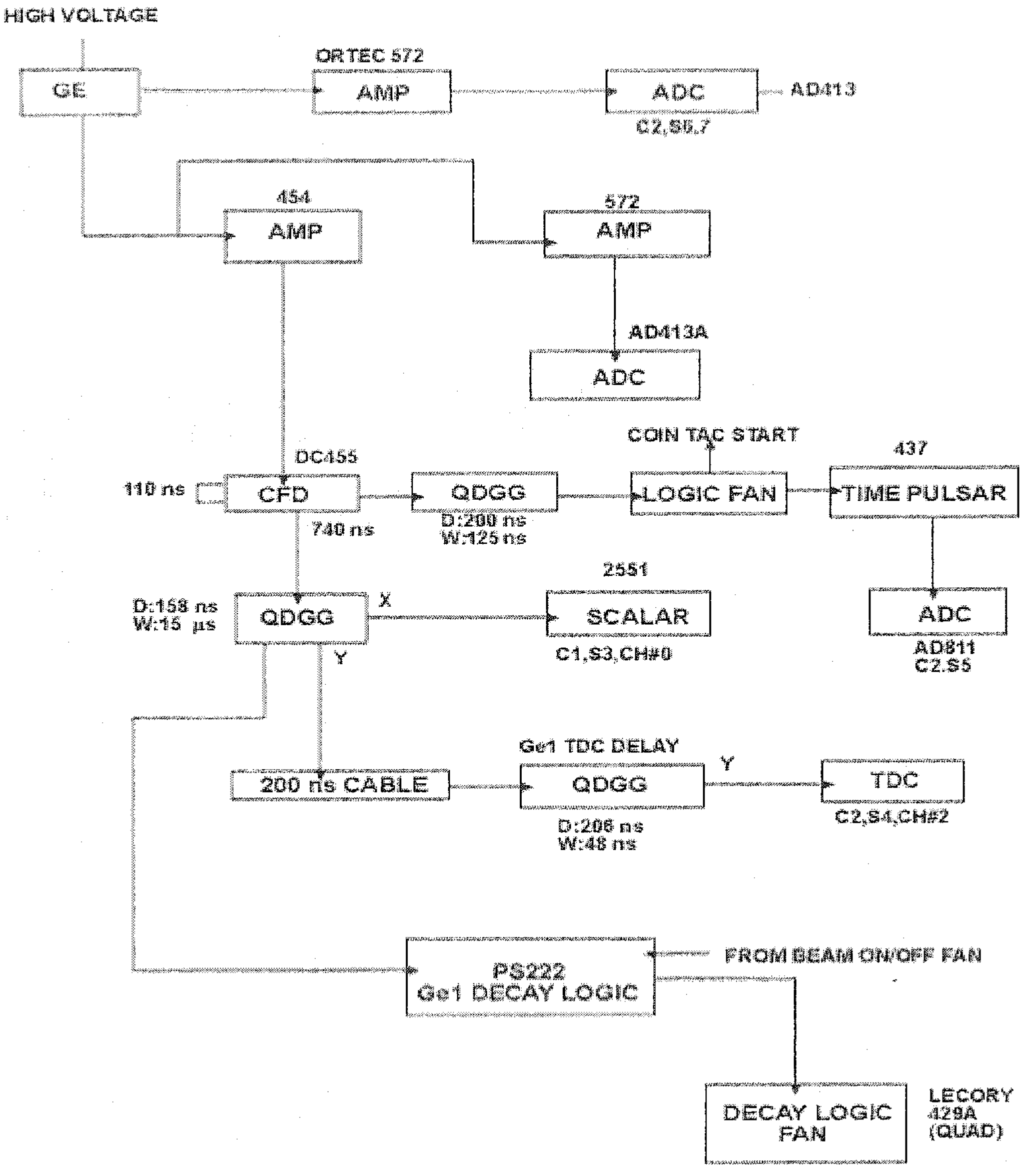
HIGH VOLTAGE
GE
ORTEC 572
AMP
ADC
AD413
C2,S5,7
454
AMP
572
AMP
AD413A
ADC
COIN TAC START
437
DC455
110 ns
CFD
QDGG
LOGIC FAN
TIME PULSAR
740 ns
D:200 ns
W:125 ns
2551
D:158 ns
W:15 µs
QDGG
X
SCALAR
ADC
Y
C1,S3,CH#0
AD811
C2,S5
Ge1 TDC DELAY
Y
200 ns CABLE
QDGG
TDC
C2,S4,CH#2
D:208 ns
W:48 ns
FROM BEAM ON/OFF FAN
PS222
Ge1 DECAY LOGIC
DECAY LOGIC
FAN
LECORY
429A
(QUAD)

Fig. A.4 Schematic diagram of the germanium detector electronics and logic circuitry.

APPENDIX B

PROGRAMMING CODE FOR THE WHEEL MOTOR CONTROL

Appendix B contains the programming code used for operating the motor of the target wheel used in the experiment that was conducted at the National Superconducting Cyclotron Laboratory (NSCL) at Michigan State University in 1998. The title of the experiment was: "Nuclear Structure in the Heavy S, Cl, and Ar". The programming code was written by Dr. Jeff Winger.

Programming Code for the Wheel Motor Control

```
*   Expt. 97011 target wheel motor control program.
*
      INTEGER MOTOR_PORT,READ_IT,WRITE_IT
      CHARACTER*80 INPUT
      COMMON /WHEEL/ MOTOR_PORT,READ_IT,WRITE_IT
      COMMON /BLK001/ INPUT

      CALL INITIALIZE
      CALL MENU

      END
*
*   INITIALIZE establishes the connection to the motor.
*
      SUBROUTINE INITIALIZE
      IMPLICIT INTEGER (A-Z)
      INTEGER MOTOR_PORT,READ_IT,WRITE_IT
      CHARACTER*80 INPUT
      CHARACTER*16 DEVICE
      INCLUDE '($IODEF)'
      INCLUDE '($SSDEF)'
      COMMON /WHEEL/ MOTOR_PORT,READ_IT,WRITE_IT
      COMMON /BLK001/ INPUT


      WRITE_IT = IO$_WRITEVBLK !
      READ_IT = IO$_READPROMPT+IO$M_NOECHO+IO$M_TIMED

      WRITE(6,100)
100   FORMAT(' Please input LTA port name for the wheel: '$)
      READ(4,200) DEVICE
200   FORMAT(A16)
      STATUS = SYS$ASSIGN(DEVICE,MOTOR_PORT,,)
      IF(STATUS.NE.SS$_NORMAL) THEN
       WRITE(6,300)
300    FORMAT('0 Error in assignment for motor controller')
       CALL EXIT(STATUS)
      END IF
      STATUS = SYS$QIOW(,%VAL(MOTOR_PORT),
     *           %VAL(IO$_TTY_PORT+IO$M_LT_CONNECT),
   *              SBLKM,,,,,,,,)
     IF(STATUS.NE.SS$_NORMAL) THEN
      WRITE(6,400)
400    FORMAT('0 Error in connection')
      CALL EXIT(STATUS)
     END IF
     WRITE(6,500)
500  FORMAT('0 Connected to Target Wheel',/,
   * '  Press Return to Continue')
     ACCEPT *

     RETURN
     END
*
*    SEND_COMMAND sends a motor controller command to the
*    Whedco controller.
*
     SUBROUTINE SEND_COMMAND
     IMPLICIT INTEGER (A-Z)
     INTEGER MOTOR_PORT,READ_IT,WRITE_IT
     CHARACTER*80 INPUT
     INCLUDE '($IODEF)'
     INCLUDE '($SSDEF)'
     BYTE COMMAND(80),MOTOR_DATA(80)
     INTEGER*2 SBLKM(4)
     INTEGER EVT_FLAG/32/,LENR/1/,IND,READ_TERM(2),DELTA_T/10/,
   *  ERROR_CONDITION
     CHARACTER*80 TEMP
     EQUIVALENCE  (TEMP,COMMAND(1))
     COMMON /WHEEL/ MOTOR_PORT,READ_IT,WRITE_IT
     COMMON /BLK001/ INPUT

10    TEMP = INPUT
     IND = INDEX(TEMP,char(13))
     READ_TERM(1) = 0
     READ_TERM(2) = '0040'X
     STATUS = SYS$QIOW(%VAL(Evt_FLAG),%VAL(MOTOR_PORT),
   *              %VAL(READ_IT),SBLKM,,,MOTOR_DATA,
   *              %VAL(LENR),%VAL(DELTA_T),READ_TERM,
   *              COMMAND,%VAL(IND))
     IF(.NOT.STATUS) THEN
      WRITE(6,100) STATUS
100    FORMAT('0 Error in reset',I4)
      CALL EXIT(STATUS)
      END IF
      IF(SBLKM(1).NE.SS$_NORMAL .AND. INPUT(3:4).NE.'CB') THEN
       IF(SBLKM(1).EQ.SS$_TIMEOUT) THEN
        WRITE(6,200) TEMP(1:IND)
200      FORMAT('0 Motor command timeout...retrying ',A<IND>)
        GOTO 10
       ELSE
        ERROR_CONDITION = SBLKM(1)
        CALL LIB$SIGNAL(%VAL(ERROR_CONDITION))
       END IF
      END IF

      RETURN
      END
*
*     MENU provides the user with callable options for interfacing
*     with the wheel.
*
      SUBROUTINE MENU
      INTEGER MOTOR_PORT,READ_IT,WRITE_IT
      CHARACTER*80 INPUT
      INTEGER OPTION
      COMMON /WHEEL/ MOTOR_PORT,READ_IT,WRITE_IT
      COMMON /BLK001/ INPUT

      OPTION = ' '
      DO WHILE(OPTION.NE.8)
10      WRITE(6,100)
100     FORMAT(1H1,4X'Expt. 97011 Target Wheel Program',/,' ',/,
     *  ' OPTIONS:',/,' ',
     *   9X,' 1. Turn wheel on',/,' ',/,
     *  10X,' 2. Turn wheel off',/,' ',/,
     *  10X,' 3. Advance to Home',/,' ',/,
     *  10X,' 4. Start wheel rotation',/,' ',/,
     *  10X,' 5. Stop wheel rotation',/,' ',/,
     *  10X,' 6. Send single commands',/,' ',/,
     *  10X,' 7. Wheel status',/,' ',/,
     *  10X,' 8. Exit program',/)
       WRITE(6,200)
200     FORMAT('  Enter Option:'$)
       READ(4,300,ERR=10) OPTION
300     FORMAT(I2)
       IF(.NOT.((OPTION.GE.1).AND.(OPTION.LE.8))) THEN
        WRITE(6,400)
```

```
400     FORMAT('0 Please enter a correct option.',/,
     *   '  Press Return to continue')
         ACCEPT *
        ELSE IF(OPTION.EQ.1) THEN
         CALL WHEEL_ON
        ELSE IF(OPTION.EQ.2) THEN
         CALL WHEEL_OFF
        ELSE IF(OPTION.EQ.3) THEN
         CALL HOME
        ELSE IF(OPTION.EQ.4) THEN
         CALL START
        ELSE IF(OPTION.EQ.5) THEN
         CALL STOP
        ELSE IF(OPTION.EQ.6) THEN
         CALL SINGLE_COMMANDS
        ELSE IF(OPTION.EQ.7) THEN
         CALL WHEEL_STATUS
        END IF
       END DO

       RETURN
       END
*
*     WHEEL_ON does a warm boot of the wheel, sets the encoder
*     ratio, and writes the profiles needed for the target
*     motion controll.
*
       SUBROUTINE WHEEL_ON
       INTEGER MOTOR_PORT,READ_IT,WRITE_IT
       CHARACTER*80 INPUT
       INTEGER COMMAND_NUMBER,TOTAL_COMMANDS/38/
       CHARACTER*10 TEMP2
       CHARACTER*10 COMMAND_LIST(38)/'M0WB','M0ER6554','M0SP445',
     * 'M0AC3600','M0DE1','M0AM111','M0RAT','M0MW','M0AM222',
     * 'M0RAT','M0MW','M0AM333','M0RAT','M0MW','M0AM444','M0RAT',
     * 'M0MW','M0AM555','M0RAT','M0MW','M0AM666','M0RAT','M0MW',
     * 'M0AM777','M0RAT','M0MW','M0AM888','M0RAT','M0MW','M0AM995',
     * 'M0RAT','M0MW','M0PFH','M0ED','M0DE2','M0EX1','M0EX2',
     * 'M0ED'/
       COMMON /WHEEL/ MOTOR_PORT,READ_IT,WRITE_IT
       COMMON /BLK001/ INPUT

       DO COMMAND_NUMBER=1,TOTAL_COMMANDS
        TEMP2 = COMMAND_LIST(COMMAND_NUMBER)
     IND = INDEX(TEMP2,' ') - 1
     INPUT = TEMP2(1:IND)//CHAR(13)
     CALL SEND_COMMAND
    END DO
    RETURN
    END
*
*    WHEEL_OFF does a cold boot of the wheel.
*
    SUBROUTINE WHEEL_OFF
    INTEGER MOTOR_PORT,READ_IT,WRITE_IT
    CHARACTER*80 INPUT
    COMMON /WHEEL/ MOTOR_PORT,READ_IT,WRITE_IT
    COMMON /BLK001/ INPUT


    INPUT = 'M0CB'//char(13)
    CALL SEND_COMMAND

    RETURN
    END
*
*    HOME moves the wheel to its home position.
*
    SUBROUTINE HOME
    INTEGER MOTOR_PORT,READ_IT,WRITE_IT
    CHARACTER*80 INPUT
    COMMON /WHEEL/ MOTOR_PORT,READ_IT,WRITE_IT
    COMMON /BLK001/ INPUT


    CALL STOP
    INPUT = 'M0MW'//char(13)
    CALL SEND_COMMAND
    INPUT = 'M0PFH'//char(13)
    CALL SEND_COMMAND

    RETURN
    END
*
*    START executes the second profile to set the wheel in
*    an infinite loop of rotations.
*
    SUBROUTINE START
```

```
      INTEGER MOTOR_PORT,READ_IT,WRITE_IT
      CHARACTER*80 INPUT
      COMMON /WHEEL/ MOTOR_PORT,READ_IT,WRITE_IT
      COMMON /BLK001/ INPUT


      CALL STOP
      CALL HOME
      INPUT = 'M0MW'//char(13)
      CALL SEND_COMMAND
      INPUT = 'M0EX2'//char(13)
      CALL SEND_COMMAND

      RETURN
      END
*
*     STOP sends the stop command to the wheel.
*
      SUBROUTINE STOP
      INTEGER MOTOR_PORT,READ_IT,WRITE_IT
      CHARACTER*80 INPUT
      COMMON /WHEEL/ MOTOR_PORT,READ_IT,WRITE_IT
      COMMON /BLK001/ INPUT
      INPUT = 'M0ST'//char(13)
      CALL SEND_COMMAND

      RETURN
      END
*
*     SINGLE_COMMNAD sends a single Whedco controller command to
*     the wheel.  The command to send is requested.
*
      SUBROUTINE SINGLE_COMMANDS
      INTEGER MOTOR_PORT,READ_IT,WRITE_IT
      CHARACTER*80 INPUT
      CHARACTER*10 COMMAND
      COMMON /WHEEL/ MOTOR_PORT,READ_IT,WRITE_IT
      COMMON /BLK001/ INPUT
      INTEGER IND

10    WRITE(6,100)
100   FORMAT('    Enter command: '$)
      READ(4,200) COMMAND
200   FORMAT(A10)
```

```
      IF(COMMAND(1:1).EQ.' ') RETURN
      IND = INDEX(command,' ') - 1
      INPUT = 'M0'//COMMAND(1:ind)//char(13)
      CALL SEND_COMMAND
      CALL WHEEL_STATUS
      GO TO 10

      END
*
*     WHEEL_STATUS prompts the controller for its status.
*
      SUBROUTINE WHEEL_STATUS
      IMPLICIT INTEGER (A-Z)
      INTEGER MOTOR_PORT,READ_IT,WRITE_IT
      CHARACTER*80 INPUT
      INCLUDE '($IODEF)'
      INCLUDE '($SSDEF)'
      BYTE COMMAND(80),MOTOR_DATA(80)
      INTEGER*2 SBLKM(4)
      INTEGER EVT_FLAG/32/,LENR/12/,IND,READ_TERM(2),DELTA_T/10/,
     * MOTOR_STATUS,ERROR_CONDITION,WHEEL_POSITION
      CHARACTER*80 TEMP,TEMP1
      EQUIVALENCE  (TEMP,COMMAND(1))
      EQUIVALENCE (TEMP1,MOTOR_DATA(1))
      COMMON /WHEEL/ MOTOR_PORT,READ_IT,WRITE_IT
      COMMON /BLK001/ INPUT
      TEMP = 'M0RS'//char(13)
      IND = INDEX(TEMP,char(13))
      READ_TERM(1) = 0
      READ_TERM(2) = '2000'X
      STATUS = SYS$QIOW(%VAL(Evt_FLAG),%VAL(MOTOR_PORT),
     *              %VAL(READ_IT),SBLKM,,,MOTOR_DATA,
     *              %VAL(LENR),%VAL(DELTA_T),READ_TERM,
     *              COMMAND,%VAL(IND))
      IF(.NOT.STATUS) THEN
        WRITE(6,100) STATUS
100       FORMAT('0 Error in reading status',I4)


        CALL EXIT(STATUS)
      ELSE
        IF(SBLKM(1).NE.SS$_NORMAL) THEN
          IF(SBLKM(1).EQ.SS$_TIMEOUT) THEN
            WRITE(6,200)
```

```
200      FORMAT('0 Motor status timeout')
       ELSE
        ERROR_CONDITION = SBLKM(1)
        CALL LIB$SIGNAL(%VAL(ERROR_CONDITION))
       END IF
      ELSE
       IND = INDEX(TEMP1,char(13))-1
       STATUS = OTS$CVT_TI_L(TEMP1(3:IND),MOTOR_STATUS,,)
       IF(.NOT.STATUS) THEN
        WRITE(6,300) (MOTOR_DATA(I),I=1,20)
300      FORMAT('0Motor status conversion error: ',20I)
       END IF
      END IF
      WRITE(6,400) MOTOR_STATUS
400    FORMAT('0 Motor Status: ',I6,/,
   *    '  Press Return to Continue')
      ACCEPT *

     END IF

     RETURN
     END
```